J. Mech. Phys. Solids 193 (2024) 105872

Contents lists available at ScienceDirect

Journal of the Mechanics and Physics of Solids

journal homepage: www.elsevier.com/locate/jmps

Electromechanics of stretchable hybrid response pressure sensors based on porous nanocomposites

Zheliang Wang [a,1], Zhengjie Li [a,1], Sungmin Sun [a], Sangjun Kim [b], Xianke Feng [a], Hongyang Shi [a], Nanshu Lu [a,b,*]

[a] Department of Aerospace Engineering and Engineering Mechanics, the University of Texas at Austin, TX 78712, USA
[b] Department of Mechanical Engineering, the University of Texas at Austin, TX 78712, USA

ARTICLE INFO

Keywords:
Flexible electronics
Pressure sensors
Porous materials
Stretch insensitive
Piezoresistivity
Capacitive

ABSTRACT

Stretchable pressure sensors are a key enabler of human-mimetic e-skin technology, with promising applications in soft robotics, prosthetics, biomimetics, and biosensors. Stretchable hybrid response pressure sensor (SHRPS) is an emerging type of soft pressure sensor that employs hybrid piezoresistive and piezocapacitive responses. A unique feature of SHRPS based on barely conductive porous nanocomposite (PNC) is its exceptional pressure sensitivity which trivializes its sensitivity to lateral stretch or shear. In this work, we experimentally characterize the electromechanical responses of SHRPS under various loading conditions and provide theoretical explanations through an equivalent circuit model. The capacitance and resistance of the PNC are described by a parallel mixing law and Archie's law, respectively. Our model can reasonably predict the responses of SHRPS. Our findings reveal that SHRPS exhibits minimal sensitivity to stretch and shear because the hybrid response mechanism is activated only under compression. The effects of PNC-electrode contact impedance and fringe effects are discussed.

1. Introduction

Electronic skins or e-skins refer to devices that mimic the properties and functionalities of human skins, such as stretchability, high mechanical toughness, tactile sensing capabilities, etc. (Yang et al., 2019). The growing interest in e-skins is due to their pivotal role in various technologies, including soft robotics, prosthetics, biomimetics, and biosensors (Wang et al., 2015; Chortos et al., 2016; Lee et al., 2019; Wang et al., 2021; Kim et al., 2018; Yao and Zhu, 2014). As the central part of the e-skin, soft pressure sensors have received extensive research, leading to the proposal of various working mechanisms, including piezoresistive, piezoelectric, triboelectric, ionic, optical and magnetic responses (Pyo et al., 2021; Chen et al., 2021; Yang et al., 2019; Wang et al., 2018; Chen and Pei, 2017; Hammock et al., 2013; Chang et al., 2021; Zhang et al., 2022). Capacitive pressure sensors (CPS) and resistive pressure sensors (RPS) stand out among these sensors due to their softness, thinness, high sensitivity, facile fabrication, and easy signal readout (Chen and Yan, 2020; Li et al., 2020a; Qin et al., 2021; Yuan et al., 2021; Yang et al., 2020b).

We start by introducing the basic constructions and equivalent circuit models for CPS and RPS. A typical soft CPS (Pyo et al., 2021; Li et al., 2020b; Qin et al., 2021; Mishra et al., 2021; Ha et al., 2022) consists of dielectric materials sandwiched between two parallel plate electrodes, as shown in Fig. 1A, where the porous nanocomposite serves as an example of a dielectric material

* Corresponding author at: Department of Aerospace Engineering and Engineering Mechanics, the University of Texas at Austin, TX 78712, USA.
E-mail address: nanshulu@utexas.edu (N. Lu).
[1] Co-first authors.

https://doi.org/10.1016/j.jmps.2024.105872
Received 1 April 2024; Received in revised form 13 August 2024; Accepted 16 September 2024
Available online 29 September 2024

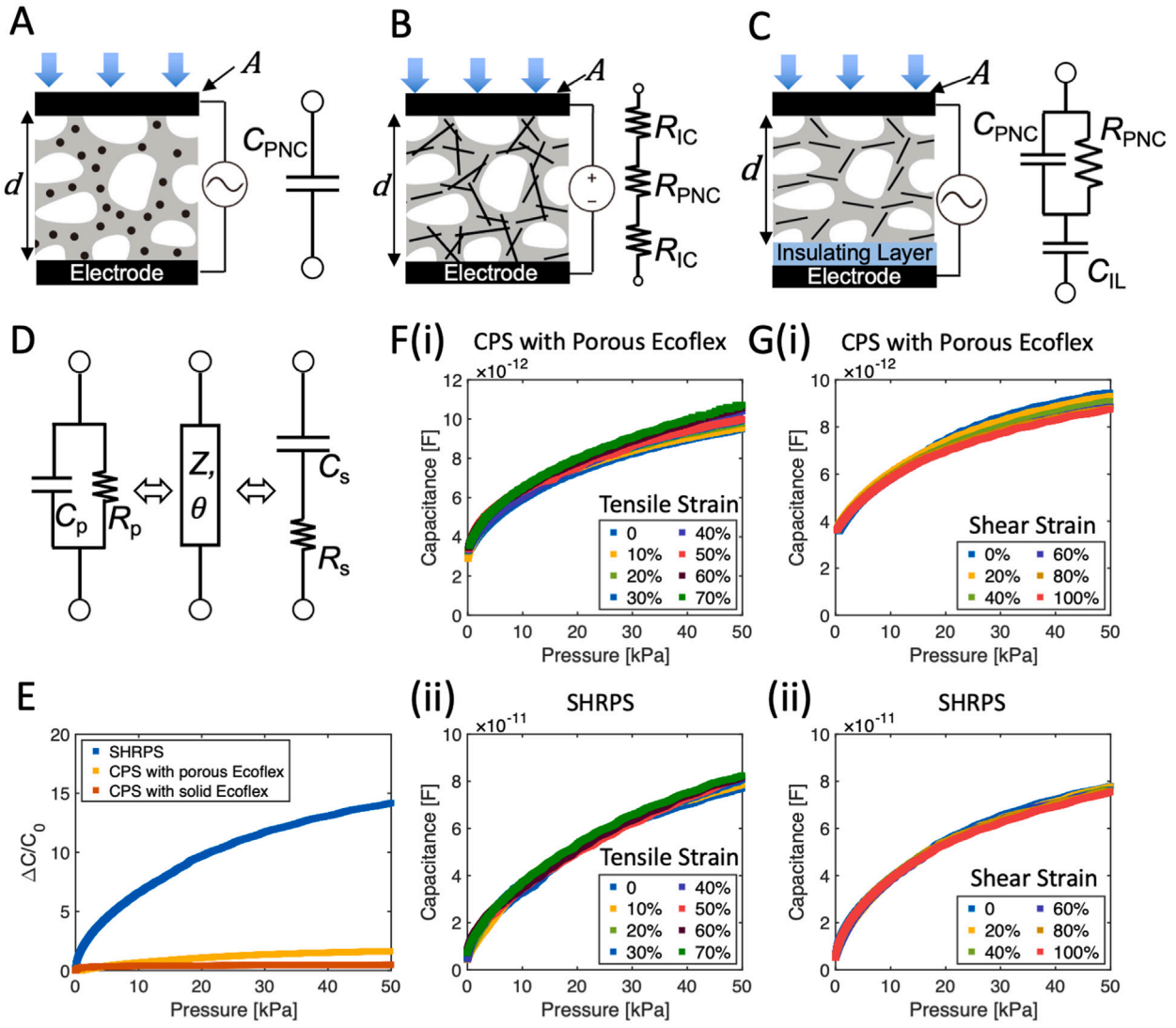

Fig. 1. (A) Schematics of a CPS based on a dielectric porous nanocomposite (PNC) and the corresponding equivalent circuit model. (B) Schematics of an RPS based on a conductive PNC and the corresponding equivalent circuit model which accounts for interface contact (IC) resistance. (C) Schematics of a hybrid response pressure sensor (HRPS) based on a barely conductive PNC and an insulating layer (IL) and the corresponding equivalent circuit model. (D) Three equivalent ways of describing a complex impedance: amplitude Z and phase angle θ (middle), parallel capacitance C_p and parallel resistance R_p (left), or serial capacitance C_s and serial resistance R_s (right). (E) SHRPS (blue markers) shows significantly improved pressure response compared to CPS with porous Ecoflex (yellow markers) or solid Ecoflex (red markers). (F) Under simultaneously applied pressure and stretch: (i) CPS with porous Ecoflex is still sensitive to stretch, especially at large pressure. (ii) SHRPS is almost insensitive to stretch. (G) Under simultaneously applied pressure and shear: (i) conventional CPS with porous Ecoflex is marginally affected by shear whereas (ii) SHRPS are not sensitive to shear.

whose dielectric constant can be tuned by high-k or conductive dopants. The corresponding capacitance is

$$C_{\mathrm{PNC}} = \epsilon_0 k_{\mathrm{PNC}} \frac{A}{d}, \tag{1}$$

where ϵ_0 is the permittivity of vacuum, k_{PNC} is the effective dielectric constant of PNC, A is the electrode area, and d is the gap distance between the two parallel electrodes. Upon compression, the capacitance would increase with the applied pressure, with the initial sensitivity, which is applicable when $P \ll E$, being defined as

$$S = \frac{d\left(\frac{\Delta C}{C_0}\right)}{dP} = \frac{1}{k_0}\left(\frac{k_{\mathrm{PNC}}}{E} + \frac{\partial k_{\mathrm{PNC}}}{\partial P}\right), \tag{2}$$

where E is the compressive modulus of the dielectric material, k_0 is the dielectric constant of the undeformed dielectric material, and P is the applied pressure (Ha et al., 2022). PNC enhances the sensitivity of CPS compared to its solid counterparts through reduced E and the dielectrostriction effect, i.e., pressure-sensitive k_{PNC} (Yang et al., 2020a).

RPS can be constructed using the same structure by employing a conductive PNC as the sandwich core (Fig. 1B). While the AC voltage must be used for capacitance measurement in CPS, DC voltage is applied for resistance measurement in RPS. The total resistance is described by the PNC resistance (R_{PNC}) and two interface contact resistances (R_{IC}) connected in series:

$$R = R_{PNC} + 2R_{IC}. \tag{3}$$

Although widely overlooked, R_{IC} is often the dominant term in R (Luo et al., 2017; Tang et al., 2020; Khalili et al., 2016) when interfacial contact has asperity. Similar to C_{PNC} in CPS, R_{PNC} is determined as

$$R_{PNC} = \rho_{PNC}\frac{d}{A}, \tag{4}$$

where ρ_{PNC} is the effective resistivity of PNC.

Despite decades of research, RPS and CPS still suffer from two major bottlenecks: the drastic decline in sensitivity with increasing pressure and the interference in pressure readings caused by in-plane stretch (Qin et al., 2021; Ha et al., 2022). Recently, we introduced a novel hybrid response pressure sensor (HRPS) (Ha et al., 2021) and its stretchable version (SHRPS) (Ha et al., 2024) that addressed both challenges. (S)HRPS exhibits piezocapacitivity and piezoresistivity simultaneously using a barely conductive PNC and a thin insulating layer as the sandwich core (Fig. 1C). Unlike CPS and RPS, the electrical properties of (S)HRPS and the barely conductive PNC can only be fully described by a complex impedance $\boldsymbol{Z} = Z\exp(i\theta)$, where Z is the magnitude of the impedance and θ is the phase angle, as shown in Fig. 1D. The electrical response is purely capacitive when $\theta = -90°$ and purely resistive when $\theta = 0°$. The complex impedance can be described equivalently using parallel capacitance $C_p = \sin\theta/(\omega Z)$ and parallel resistance $R_p = Z/\cos\theta$, or alternatively, serial capacitance $C_s = 1/(\omega Z\sin\theta)$ and serial resistance $R_s = Z\cos\theta$, where ω is the applied AC frequency.

The simplest equivalent circuit model for (S)HRPS comprises the resistance of the PNC R_{PNC}, the capacitance of the PNC C_{PNC}, and the capacitance of the insulating layer C_{IL} (Fig. 1C). The insulating layer is designed to be ultrathin compared to PNC, $C_{IL} \gg C_{PNC}$. When the PNC is undeformed, current flows predominantly through the capacitive branch due to the large initial resistance, resulting in a phase angle close to $-90°$ and a total capacitance close to C_{PNC}. Upon compression, R_{PNC} experiences a significant decrease, causing more current to flow through the resistive branch, and eventually the total serial capacitance of the sensor would approach C_{IL}. This hybrid response mechanism produces a markedly enhanced sensitivity in HRPS serial capacitance compared to traditional CPS systems based on solid or porous dielectric materials (Fig. 1E). In fact, the sensitivity of HRPS exceeds that of other capacitive pressure sensors reported in the last decade in the pressure range above 3 kPa (Ha et al., 2021). HRPS can be made stretchable by using stretchable electrodes, stretchable insulating layers, and a tougher PNC (Ha et al., 2024). SHRPS inherits the sensitivity of HRPS and achieves a stretchability of 70%, an unprecedented combination in the existing literature. Fig. 1F(i)–(ii) illustrates the serial capacitance of CPS with porous Ecoflex and SHRPS under simultaneous pressure and stretch. Although CPS with porous Ecoflex is less affected by in-plane stretch interference as shown in Fig. 1F(i) compared to their counterpart with solid Ecoflex (Ha et al., 2024), a relative error of up to 20% persists. In contrast, SHRPS is almost free of stretch interference, as the response to pressure overwhelms that to stretch, causing the capacitance curves under various tensile strains to almost overlap in Fig. 1F(ii). Fig. 1G(i)–(ii) illustrates the serial capacitance of CPS with porous Ecoflex and SHRPS under simultaneous pressure and shear. The CPS with porous Ecoflex shows less shear sensitivity compared to stretch, with a maximum error of 10%, while SHRPS is almost free from shear interference due to the overwhelming pressure response.

Despite its success, the fundamental understanding of the electromechanics of SHRPS remains elusive. Similar to CPS and RPS, modeling k_{PNC} and ρ_{PNC} under various deformation conditions is the key to elucidating the electromechanical responses of SHRPS. PNC can be treated as a two-phase composite of air and nanocomposites. The effective physical properties of PNC can thus be modeled using the properties of air and nanocomposites along with their volume fraction ratio. Numerous empirical rules of mixtures or theories of effective medium have been proposed to predict the capacitance of composites, including the parallel model, the perpendicular model, Maxwell–Garnett theory, Bruggeman theory, Hashin–Shtrikman bounds, and others (Choy, 2015). However, their application to PNC or PNC-based CPS has not been well studied. Most researchers adopt a simple parallel model without justification, where $k_{PNC} = \phi k_{air} + (1-\phi)k_{NC}$, with ϕ denoting porosity (Atalay et al., 2018; Ruth et al., 2020; Lv et al., 2023). Although the same models can be applied to obtain effective resistivity, Archie's law is more pertinent to PNC modeling. Archie's law is an empirical model widely used to relate the conductivity of a porous rock to its porosity (Archie, 1942; Glover, 2015). Recently, it has been applied successfully to model RPS based on conductive PNC (Zhang et al., 2021). However, its applicability to barely conductive PNC and other loading conditions has not been studied. At the sensor level, although an equivalent circuit model has been proposed by Ha et al. (2024) to model the pressure response of SHRPS, its applicability to other loading conditions has not been tested. Moreover, the equivalent circuit model is based on a fitting parameter obtained through multiscale modeling that cannot be experimentally verified. In addition, investigations of possible factors that might affect experimental readings are lacking, including parasitic capacitance, fringe effects, and contact resistance.

In this work, we conduct electromechanical characterizations of both PNC and SHRPS under various loading conditions and always use the undoped porous polymer as the benchmarking specimens. A rigorous protocol was developed to calibrate parasitic capacitance and fringe effects. Both SHRPS and barely conductive PNC are found to be highly sensitive to compression, much less sensitive to in-plane stretch, and almost insensitive to shear. The parallel capacitance of PNC is modeled using the parallel model and is compared to other mixing laws. The parallel resistance of PNC is well captured using a directional Archie's law. A new equivalent circuit model for SHRPS is proposed that eliminates the need for multiscale modeling. The proposed model is capable of capturing the electromechanical response of SHRPS under all loading conditions tested. The analytical framework established in this work can shed light on all resistive, capacitive, and hybrid response pressure sensors operating under AC voltage. The fundamental electromechanical understanding of SHRPS achieved in this work is useful for the future design and application of SHRPS.

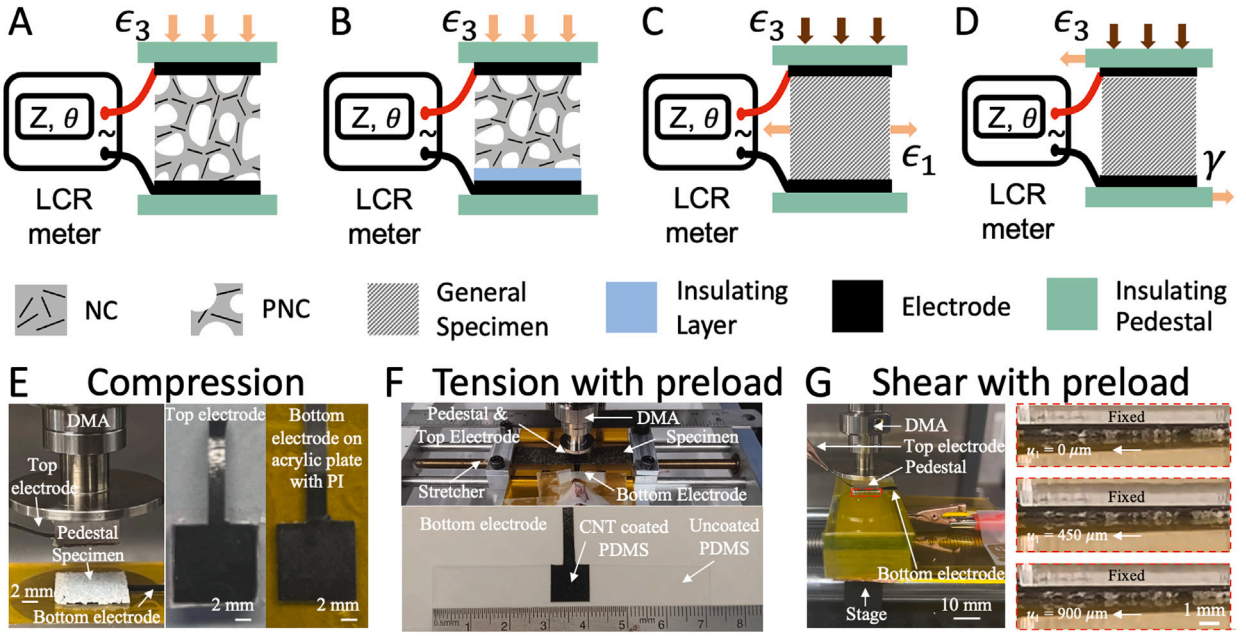

Fig. 2. Schematics of the electromechanical characterizations of (A) a PNC under compression, (B) an insulated PNC under compression, (C) a general specimen under tension with preload, and (D) a general specimen under shear with preload. Photos for the experimental setups of (E) compression test and close-ups for top and bottom electrodes, (F) tension test and a close-up for the bottom electrode, and (G) shear test and cross-sectional views for the undeformed and deformed specimens.

2. Methods

2.1. Sample preparation

We followed the procedures in our previous work to fabricate stretchable electrodes made of carbon nanotubes (CNTs) sprayed on polydimethylsiloxane (PDMS) and the PDMS insulating layer (Ha et al., 2024). Our methodology began with the fabrication of the CNT-PDMS electrodes incorporating an insulating layer. This process involved preparing a diluted mixture of PDMS (base-to-curing agent ratio 10:1) and hexane at a weight ratio of 1:4. The mixture was then spin-coated onto a polyimide (PI) substrate (Aiyunni Polyimide) at a speed of 6000 rpm for one minute. Subsequent curing on a hot plate at 100 °C for 30 min allowed solidification of the PDMS insulating layer, which was then cut using a razor blade to ensure the proper area for insulating. After the fabrication of the insulating layer, a rectangular PI mask (60 × 10 mm^2) was applied to the insulating layer, and a mixture of CNTs in chloroform (at a mixing ratio of 1 mg CNT to 1 ml chloroform), previously sonicated using a Q500 sonicator (QSonia), was spray-coated selectively onto a 10 mm-wide area on the specimen. This coating process took place while the sample was heated on a hot plate at 100 °C to facilitate rapid chloroform evaporation. After removal of the mask, another layer of PDMS (10:1) was spin-coated at 1000 rpm for 45 s and then cured in an oven at 70 °C for 2 h. A water-soluble tape (SmartSolve) was applied as a backing layer using a roller. This assembly, which consists of the backing layer and the electrode layer embedded with CNT-PDMS, was then carefully detached from the PI substrate. The final step involved removing the water-soluble backing layers by soaking them in water and gentle rubbing, thereby completing the fabrication of the CNT-PDMS electrode with an insulating layer. The process for fabricating the CNT-PDMS electrode without the insulating layer followed the same steps, with the exception of the insulating layer fabrication stage.

We employed a well-established material preparation method to fabricate nanocomposites (NC) and porous nanocomposites (PNC) as outlined in previous works (Ha et al., 2021, 2024). Specifically, 120 mg of hydroxyl-functionalized multiwall carbon nanotubes (Carbon Nanotubes Plus) was dispersed in 240 mL of chloroform (Sigma-Aldrich). The dispersion underwent ultrasonication using a Q500 sonicator (QSonica) at 500 watts for 10 min. Subsequently, 30 g of the uncured Ecoflex (Ecoflex 00–30, Smooth-on) base polymer was integrated into the dispersion, followed by another round of sonication for 10 min. To remove the chloroform, the mixture was then heated and agitated at 100 °C and 400 rpm using a magnetic stirrer (Fisher Scientific) until the chloroform to Ecoflex weight ratio was reduced to 10:1. For the fabrication of NC, a conductive silicon wafer (University Wafer) with dimensions of 20 × 15 mm^2 was used as a template. It was dip-coated into the solution for 5 s, withdrawn, and then placed on a 150 °C hotplate for 10 min to completely evaporate the chloroform. This dip-coating process was repeated once before curing in a 150 °C oven. For PNC fabrication, a nickel foam template was used instead of a silicon wafer, following the same dip-coating protocol as for NC. After curing, the specimens were etched in 3 M hydrochloric acid (HCl, Sigma-Aldrich) at 80 °C for 12 h to dissolve the nickel foam template, followed by rinsing with distilled water.

Table 1
The experimental setups investigated in this paper and their abbreviations.

Doping	Insulating layer	Loading
Undoped porous polymer (U)	Without insulating layer (P)	Compression (C)
Doped PNC (D)	With insulating layer (I)	Tension (T)
		Shear (S)

2.2. Electromechanical characterizations

2.2.1. Morphology measurement

After curing, we first measured the thickness of the NC film and the wall thickness of the PNC ligaments. This step was crucial to ensure that the electrical properties measured in the NC film are representative of nanocomposites in the PNC since the electrical properties of the conductive-filler composites may be thickness-dependent (Fu et al., 2009; Li et al., 2016, 2019; Lin et al., 2010). The thickness of the fabricated NC film was ~ 20 μm, as estimated from the weight and density of NC. The average wall thickness of the PNC ligaments was 22.49 μm (average of 20 ligaments, 3 ligaments were shown in Fig. 12B), determined by optical profilometer (VK-X1100, Keyence), which was comparable to the fabricated NC film. The total thickness of the PNC specimen was measured to be around 0.9 mm using a caliper.

2.2.2. NC film characterization

NC were cut into a 11 × 11 mm^2 square shapes using a metallic cutter. CNT-PDMS electrodes were cut into a 10 × 10 mm^2 square with a 2 mm wide tail for connection before the experiment. The characterization of the electrical properties of the nanocomposite (NC) involved a series of meticulously planned steps. Initially, an 11 × 11 mm^2 NC sample was placed on a conductive wafer with dimensions of 20 × 15 mm^2 (Length × Width). This assembly was placed under a Dynamic Mechanical Analyzer (Abbreviated as DMA, RSA-G2, TA Instruments), where a CNT-PDMS electrode was attached to DMA and used as the top electrode, while the conductive wafer functioned as the bottom electrode. DMA could control the gap between the electrodes, precisely adjusted to match the thickness of the NC. The electrodes were then interconnected to an LCR meter (3532-50, Hioki) to measure impedance by applying an alternating current (AC) signal with a frequency of 1 kHz and voltage of 2 V. The same frequency and voltage were used for all subsequent experiments, avoiding any potential frequency-dependent behavior (Li et al., 2022).

2.2.3. PNC characterization

In this study, we conducted electromechanical characterizations encompassing two types of constituent materials, two specimen configurations, and three loading conditions, resulting in a total of 12 setups (2 × 2 × 3). The constituent materials investigated include an undoped porous polymer and a doped PNC with a doping ratio of 0.4 wt%, abbreviated U and D, respectively. The undoped specimens are purely capacitive and represent the CPS, while the doped specimens exhibit a hybrid response. The two specimen configurations involve the characterization of PNC using a bottom electrode with and without an insulating layer, abbreviated as I and P respectively. The behavior of the doped and insulated PNC corresponds to the SHRPS previously developed in our work. Three common types of loading encountered in soft pressure sensors were investigated: out-of-plane compression (C), in-plane tension (T), and shear (S). In this work, we will focus on the cases listed in Table 1.

In compression and shear tests, the PNC were cut into squares of 11 × 11 mm^2. A DMA (RSA-G2, TA Instruments) and an LCR meter (3532-50, Hioki) were used to record both compressive force and displacement, which were then converted to pressure and strain. Impedance and phase angle were measured *in situ* using the LCR meter. To mitigate electromagnetic noise, dielectric acrylic layers were implemented (Fig. S1). Specifically, a 10 × 10 × 8 mm^3 (Length × Width × Height) acrylic pedestal and a 200 × 50 × 2 mm^3 acrylic substrate were affixed to the DMA's top and bottom compression fixtures, respectively (As shown in Fig. 2E). Additionally, the guard port of the LCR meter was connected to the DMA to further reduce interference (Not shown in Fig. 2E). For the testing procedure, 10 × 10 mm^2 square electrodes with tails were precisely aligned and secured to both the top and bottom acrylic layer. These electrodes were then connected to the LCR meter using two cables. PNC specimens were compressed until force reached nearly 5 N by DMA with a loading speed of 0.002 mm/s.

The stretch experiment was conducted using a stretcher apparatus and an LCR meter (3532-50, Hioki). To avoid edge effects due to clamping and nonuniform deformation, a different batch of PNC with a larger size was cut into long strips with a width of 11 mm. The long-strip CNT-PDMS electrode with a 10 × 10 mm^2 coated area was first attached to a Tegaderm film (3M), which was then attached to the stretcher. A 65 × 11 mm^2 specimen was then placed on the electrode, and the two ends of the specimen, including the bottom electrode were securely clamped by the stretcher (Fig. 2F). The top electrode was then attached to the pedestal (Fig. 2F). To ensure contact between the top electrodes and the specimen, the gap distance was determined by applying a 0.004 N preload to the unstretched specimen and maintained constant throughout the test. The specimen and bottom electrodes were incrementally stretched from 0% to 70%, with impedance data recorded at each step.

The setup for the shear experiment mirrored that of the stretch test, with the bottom electrode mounted on a stage and the top electrode affixed to a pedestal. We used the same specimens and electrodes of the same dimensions as in the compression test. The sample was placed between the electrodes at the set gap distance, and the stage was sheared from 0% to 100%. Impedance data were collected throughout the experiment (Fig. 2G).

A calibration test was essential to calibrate the unavoidable systematic errors, including the inherent parasitic capacitance between the coaxial cables connected to the LCR meter and the electrode tails (Dascher, 1996) and the fringe effect caused by the surrounding air. We first placed the electrodes with only air in between and then lowered the DMA to measure the distance and experimental capacitance values of the DMA and LCR meter. Using the known dielectric constant of air, along with the electrode area and the gap distance of DMA, we could calculate the theoretical air capacitance. The discrepancy between this theoretical value and the experimentally measured capacitance served as a measurement of systematic errors, which account for parasitic capacitance, fringe effects, and other potential errors. The systematic error changes little throughout the testing process, consistent with our assumption that the parasitic capacitance remains constant and the simulation results on the fringe effects (as described in the Discussion). In results section, the value for systematic error will be added to the theoretical value and compared to the raw experimental data. Similar calibration tests were also conducted for tensile and shear experiments with PNC replaced by air. The measured systematic error is included in the Supplementary Information (Tab. S1).

2.3. Ogden-Storakers model

In this work, the equivalent circuit will be constructed to relate the electrical properties of the specimens to the applied compressive, tensile, and shear strains. A constitutive model is necessary to further relate the strains with the stresses, especially the pressure. In this work, we chose the Ogden–Storakers model due to its wide application for foams. The Ogden–Storakers model is a phenomenological model and has been built into ABAQUS as the "hyperfoam" model (Storåkers, 1986). The free energy of the Ogden–Storakers model is written as follows:

$$\Psi = \sum_{i=1}^{i=N} \frac{2\mu_i}{\alpha_i^2}\left[\lambda_1^{\alpha_i} + \lambda_1^{\alpha_2} + \lambda_1^{\alpha_3} - 3 + \frac{1}{\beta_i}\left(J^{-\alpha_i\beta_i} - 1\right)\right], \tag{5}$$

where λ_1, λ_2, and λ_3 are the three principal stretches, $J = \lambda_1\lambda_2\lambda_3$, and μ_i, α_i and β_i are fitting parameters. μ_i has the units of modulus and is related to the initial shear modulus of the material μ_0 as $\mu_0 = \sum_{i=1}^{i=N} \mu_i$. β_i is related to the compressibility and Poisson's ratio. When $\beta_i = 0$ for all terms, we have a Poisson's ratio of 0. The principal Cauchy stresses are given as:

$$\sigma_a = J^{-1}\lambda_a \frac{\partial \Psi}{\partial \lambda_a} = \sum_{i=1}^{i=N} \frac{2\mu_i}{J\alpha_i}[\lambda_a^{\alpha_i} - J^{-\alpha_i\beta_i}]. \tag{6}$$

2.4. Equivalent circuit model

This section considers the electromechanical response of PNC and insulated PNC under compressive strain ϵ_3, in-plane tensile strain ϵ_1, and shear strain γ. The parallel capacitance and parallel resistance of the PNC and the insulated PNC are expressed as functions of applied strains, which can be further related to pressure.

2.4.1. Kinematics

Consider a SHRPS with a PNC layer of initial thickness d_0 sandwiched between two square electrodes of width a_0 (Fig. 3A). This section discusses changes in the effective electrode area, PNC thickness, and porosity under compression, tension, and shear.

In general, the electrode area is affected by pressure through Poisson's effect. However, the PNC in our sensor is orders of magnitude softer than the electrode, causing the normal strain and the corresponding area change in the electrodes to be negligible. Therefore, we consider the normal strain in the electrodes zero and the electrode area independent of the applied compressive strains (Fig. 3B):

$$A^{\text{compression}} = A_0 = a_0^2. \tag{7}$$

In our experimental setup for tensile tests, to avoid air trapping in assembled samples, the top electrode is fixed to the rigid pedestal and, therefore, does not deform. In contrast, the bottom electrode is under the same uniaxial tension as the PNC, deforming into a rectangle with length $a_1 = a_0(1+\epsilon_1)$ and width $a_2 = a_0(1+\epsilon_2)$, where ϵ_1 is the applied tensile strain and $1+\epsilon_2 = (1+\epsilon_1)^{-1/2}$ is the stretch in the orthogonal in-plane direction considering the incompressibility of the electrodes (Fig. 3C). In this work, we define the effective area A_{eff} as the overlapping area of the two electrodes. A_{eff} will be used to calculate the sensor capacitance in the following sections, which can be expressed as:

$$A_{\text{eff}}^{\text{tension}} = a_0 a_2 = A_0(1+\epsilon_1)^{-1/2}. \tag{8}$$

Similar to the compression test, it is assumed that the electrode is not deformed during the shear test due to the softness of PNC. However, the projection of the top electrode is displaced by $d_0\gamma$ due to applied shear strain γ. As a result, the effective electrode area under shear is expressed as:

$$A_{\text{eff}}^{\text{shear}} = a_0(a_0 - d_0\gamma) = A_0(1 - \gamma d_0/a_0). \tag{9}$$

The above equations can be written in a unified manner as:

$$A_{\text{eff}} = A_0(1+\epsilon_1)^{-1/2}\left(1 - \gamma\frac{d_0}{a_0}\right). \tag{10}$$

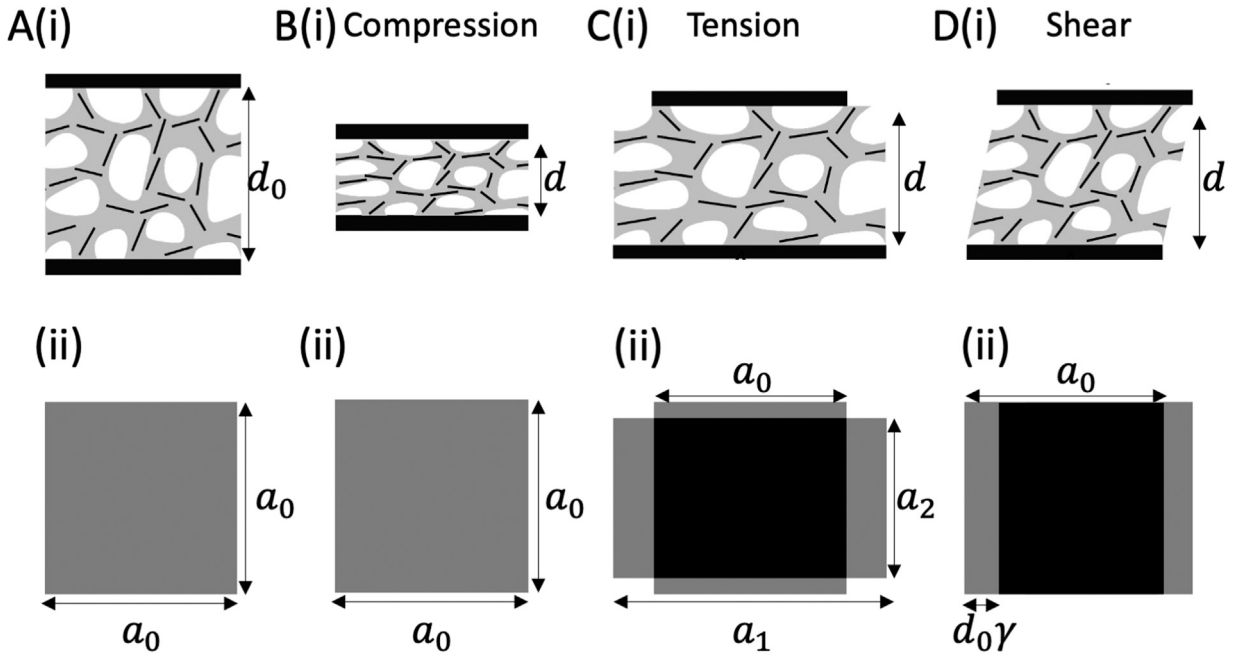

Fig. 3. Schematics of the side view (top row) and top view (bottom row) of experimental set-up under (A) undeformed configuration, (B) compression, (C) tension with undeformed top electrode, and (D) shear. The dark area in the top views indicates the overlapping electrode area.

For all tests, the DMA experimentally measures the thickness of the deformed PNC d when the pedestal with the top electrode touches the PNC. The PNC thickness is related to the compressive strain ϵ_3 as:

$$d = d_0(1-\epsilon_3). \tag{11}$$

Assuming that the solid NC is incompressible, we can calculate the porosity after deformation as:

$$\phi = 1 - \frac{(1-\phi_0)V_{\mathrm{PNC},0}}{V_{\mathrm{PNC}}} = 1 - \frac{(1-\phi_0)}{(1+\epsilon_1)(1+\epsilon_2)(1-\epsilon_3)}, \tag{12}$$

where ϕ_0 is the initial porosity, $V_{\mathrm{PNC},0}$ and V_{PNC} is the volume of the PNC in the initial and deformed configuration, respectively. The initial porosity is calculated by dividing the weight of PNC by the density of Ecoflex and the volume of the PNC. In this work, we assume the Poisson's ratio of PNC to be zero, and the expression for porosity is reduced to

$$\phi = 1 - \frac{(1-\phi_0)A_0 d_0}{A_0(1+\epsilon_1)d_0(1-\epsilon_3)} = 1 - \frac{(1-\phi_0)}{(1+\epsilon_1)(1-\epsilon_3)}. \tag{13}$$

The assumption of zero Poisson's ratio is applicable to many foam materials, (Casavola et al., 2022; Pierron, 2010), and also consistent with our observation of negligible lateral expansion of PNC during compression tests (Fig. S1). The potential influence of non-zero Poisson's ratio is discussed in the Supplementary Information.

2.4.2. Equivalent circuit model for PNC

The electrical properties of PNC are described using a parallel resistance R_{PNC} and a parallel capacitance C_{PNC} (Fig. 4A). We assume that C_{PNC} consists of an air capacitance C_{air} and an NC capacitance C_{NC} in parallel, each of which has a thickness equal to the PNC thickness and area proportional to their volume fraction:

$$C_{\mathrm{PNC}} = C_{\mathrm{air}} + C_{\mathrm{NC}}, \quad C_{\mathrm{air}} = \frac{\epsilon_0 k_{\mathrm{air}} A_{\mathrm{eff}} \phi}{d}, \quad C_{\mathrm{NC}} = \frac{\epsilon_0 k_{\mathrm{NC}} A_{\mathrm{eff}}(1-\phi)}{d}, \tag{14}$$

where A_{eff} is the effective area of the electrode obtained from Eq. (10), d is the deformed PNC thickness obtained from Eq. (11), ϕ is the porosity obtained from Eq. (13), and k_{air} and k_{NC} are the dielectric constant of air and NC, respectively. Eq. (14) can be rewritten in terms of effective dielectric constant:

$$C_{\mathrm{PNC}} = \epsilon_0 k_{\mathrm{eff}} \frac{A_{\mathrm{eff}}}{d}, \quad k_{\mathrm{eff}} = \phi k_{\mathrm{air}} + (1-\phi)k_{\mathrm{NC}}. \tag{15}$$

In this work, k_{air} is taken to be 1, and k_{NC} is 2.3 for undoped polymer and 6.0 for doped NC as obtained from the characterization of a thin NC film. The intrinsic dielectrostriction effect of NC is neglected, and k_{NC} is assumed to be constant. The proposed parallel model is compared to other possible mixing laws for PNC in the discussion section.

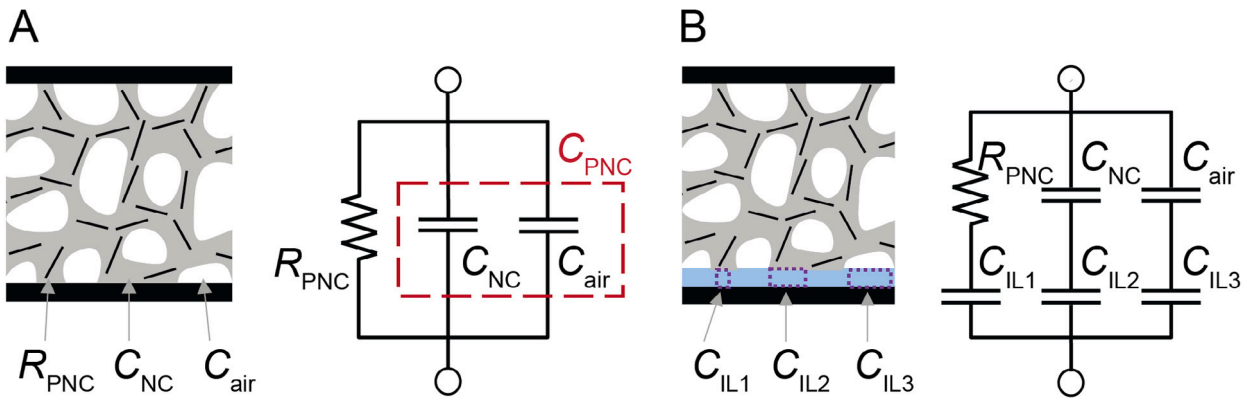

Fig. 4. Proposed equivalent circuit model for (A) uninsulated porous nanocomposite (PNC) and (B) insulated PNC or SHRPS.

We assume that the resistivity of PNC follows a directional Archie's law. The original Archie's law states that (Archie, 1942):

$$\rho_{PNC} = \rho_0 \eta^m, \tag{16}$$

where ρ_{PNC} is the effective resistivity of the PNC, ρ_0 and m are the two fitting parameters, and $\eta = 1 - \phi$ is the volume fraction of the conductive phase. Motivated by experimental observation, we assume in this work that Archie's law is directional, i.e., the resistance changes only in compression, not in tension. This directional law can be explained by the fact that compression induces contact between ligaments while tension does not, causing a distinct resistance change. The resistance of the PNC can be written as:

$$R_{PNC} = R_0 \left(1 - \epsilon_3\right)^n, \tag{17}$$

where R_0 is the initial resistance of the PNC. R_0 and n are determined using a linear least square fitting to log(R) and log$(1 - \epsilon_3)$.

2.4.3. Equivalent circuit model for insulated PNC

For the insulated PNC, we assume that R_{PNC}, C_{NC}, and C_{air} each connect to a capacitor in serial (Fig. 4B) named C_{IL1}, C_{IL2}, and C_{IL3}, respectively. Physically, C_{IL1}, C_{IL2}, and C_{IL3} represent the portion of the insulating layer that is connected to the CNTs, Ecoflex matrix in the NC, and the air, respectively. They can be evaluated as:

$$C_{IL1} = \epsilon_0 k_{PDMS} \frac{A_{IL1}}{t_{IL}}, \quad C_{IL2} = \epsilon_0 k_{PDMS} \frac{A_{IL2}}{t_{IL}}, \quad C_{IL3} = \epsilon_0 k_{PDMS} \frac{A_{IL3}}{t_{IL}}, \tag{18}$$

where $k_{PDMS} = 2.8$ is the effective dielectric constant of PDMS, $t_{IL} = 2$ μm is the thickness of the insulating layer, and $A_{IL1}, A_{IL2}, A_{IL3}$ are the effective areas for the C_{IL1}, C_{IL2}, C_{IL3}. For consistency, we should have $A_{IL1} + A_{IL2} + A_{IL3} = A_{eff}$. We assume that the effective area of IL connected to air is proportional to the porosity, i.e.,

$$A_{IL3} = A_{eff}\phi. \tag{19}$$

We followed our previous work (Ha et al., 2024) and assumed that:

$$A_{IL1} = A_{eff}(1 - \phi)\chi^{2/3}, \tag{20}$$

where χ is the volume fraction ratio of CNT in the NC converted from the weight fraction. And accordingly we have:

$$A_{IL2} = A_{eff}(1 - \phi)(1 - \chi^{2/3}). \tag{21}$$

Other possible equivalent circuit models and the necessity to split the insulating layer into multiple components will be discussed in Section 4.1. All parameters used in the proposed equivalent circuit model is summarized in Table 2.

Following the equivalent circuit in Fig. 4B, the complex impedance of the proposed model can be calculated as:

$$Z = \left[i\omega \frac{C_{air} C_{IL3}}{C_{air} + C_{IL3}} + i\omega \frac{C_{NC} C_{IL2}}{C_{NC} + C_{IL2}} + (R_{PNC} + 1/i\omega C_{IL1})^{-1} \right]^{-1}. \tag{22}$$

Other electrical properties of interest in this work, including the impedance magnitude, phase angle, parallel and serial capacitance, parallel resistance, can be derived from Z as:

$$Z = R_{PNC} \left[\left(\frac{\omega^2 C_{IL1}^2 R_{PNC}^2}{1 + \omega^2 C_{IL1}^2 R_{PNC}^2} \right)^2 + \omega^2 R_{PNC}^2 \left(\frac{C_{air} C_{IL3}}{C_{air} + C_{IL3}} + \frac{C_{NC} C_{IL2}}{C_{NC} + C_{IL2}} + \frac{C_{IL1}}{1 + \omega^2 C_{IL1}^2 R_{PNC}^2} \right)^2 \right]^{-1/2}. \tag{23}$$

Table 2
Parameters of the equivalent circuit model for PNC and insulated PNC.

Parameter	Physical significance	Value
a_0	Width of square electrode	10 mm
d_0	Initial thickness of PNC	0.9 mm 0.785 (undoped PNC)
ϕ_0	Initial porosity of PNC	0.906 (doped PNC, compression & shear) 0.878 (doped PNC, tension)
k_{air}	Dielectric constant of air	1.0
k_{NC}	Dielectric constant of NC	2.3 (undoped)/6.0 (doped)
R_0	Initial resistance of PNC	Inf (undoped)/7.93 GΩ (doped)
n	Power in the resistance–strain relationship	NA (undoped)/4.72 (doped)
t_{IL}	Thickness of insulating layer	2 μm
k_{PDMS}	Dielectric constant of PDMS	2.8
χ	Volume fraction ratio of CNT in NC	0 (undoped)/0.00329 (doped)

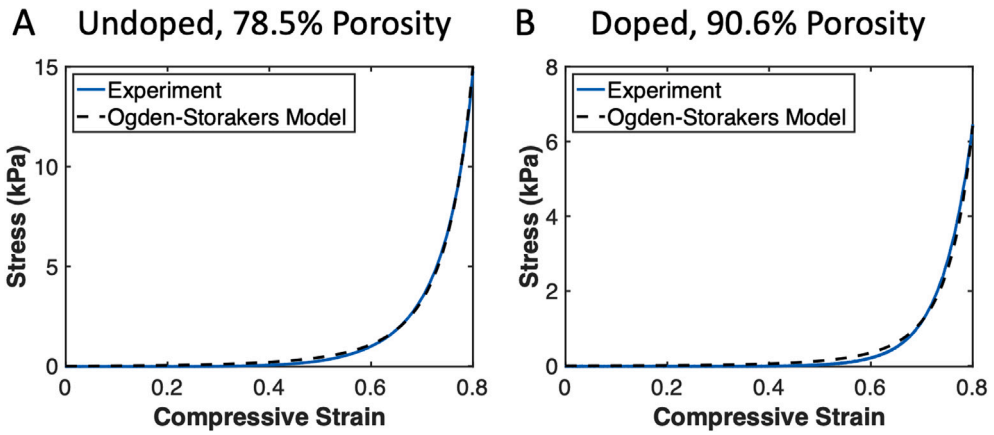

Fig. 5. Stress–strain curves of (A) undoped and (B) doped PNC under compression (solid curves) and the comparison to the Ogden–Storakers model with $N = 1$ (dashed curves).

$$\theta = \arctan\left[\omega R_{PNC}\frac{1+\omega^2 C_{IL1}^2 R_{PNC}^2}{\omega^2 C_{IL1}^2 R_{PNC}^2}\left(\frac{C_{air}C_{IL3}}{C_{air}+C_{IL3}}+\frac{C_{NC}C_{IL2}}{C_{NC}+C_{IL2}}+\frac{C_{IL1}}{1+\omega^2 C_{IL1}^2 R_{PNC}^2}\right)\right]. \tag{24}$$

$$C_p = \frac{C_{air}C_{IL3}}{C_{air}+C_{IL3}}+\frac{C_{NC}C_{IL2}}{C_{NC}+C_{IL2}}+\frac{C_{IL1}}{1+\omega^2 C_{IL1}^2 R_{PNC}^2}. \tag{25}$$

$$R_p = R_{PNC}\left(1+\frac{1}{\omega^2 C_{IL1}^2 R_{PNC}^2}\right). \tag{26}$$

$$C_s = \frac{C_{air}C_{IL3}}{C_{air}+C_{IL3}}+\frac{C_{NC}C_{IL2}}{C_{NC}+C_{IL2}}+C_{IL1}\frac{\frac{C_{air}C_{IL3}}{C_{air}+C_{IL3}}+\frac{C_{NC}C_{IL2}}{C_{NC}+C_{IL2}}+C_{IL1}}{C_{IL1}+\left(1+\omega^2 C_{IL1}^2 R_{PNC}^2\right)\left(\frac{C_{air}C_{IL3}}{C_{air}+C_{IL3}}+\frac{C_{NC}C_{IL2}}{C_{NC}+C_{IL2}}\right)}. \tag{27}$$

Sensitivity can also be derived by plugging in the above C_p or C_s into the definition in Eq. (2), which is included in the Supplementary Information.

3. Results

3.1. Stress strain curves

Fig. 5 plots the stress–strain curves of the doped and undoped PNC under compression. A typical foam exhibits a three-stage stress–strain curve under compression, including the initial linear stage, a plateau stage corresponding to the buckling of the ligaments, and a stiffening stage corresponding to the densification of the foam. Our specimen has no clear initial linear stage, probably because the critical force for buckling is below the resolution of the DMA. A long plateau region is observed, followed by a steep stiffening when the compressive strain exceeds 40%. The Ogden–Storakers model is used to fit the stress–strain curves through the non-linear least-square fitting (Fig. 5). β_i were kept zero since the lateral strain data was unavailable. It was found that $N = 1$ already gives a satisfying fitting to the experiments, where $\alpha_1 = -1.352$ and $\mu_1 = 0.1046$ kPa for doped PNC and $\alpha_1 = -1.432$ and $\mu_1 = 0.1352$ kPa for undoped PNC. While increasing N would further increase the fitting accuracy, the resultant parameters are more likely to be over-fitted.

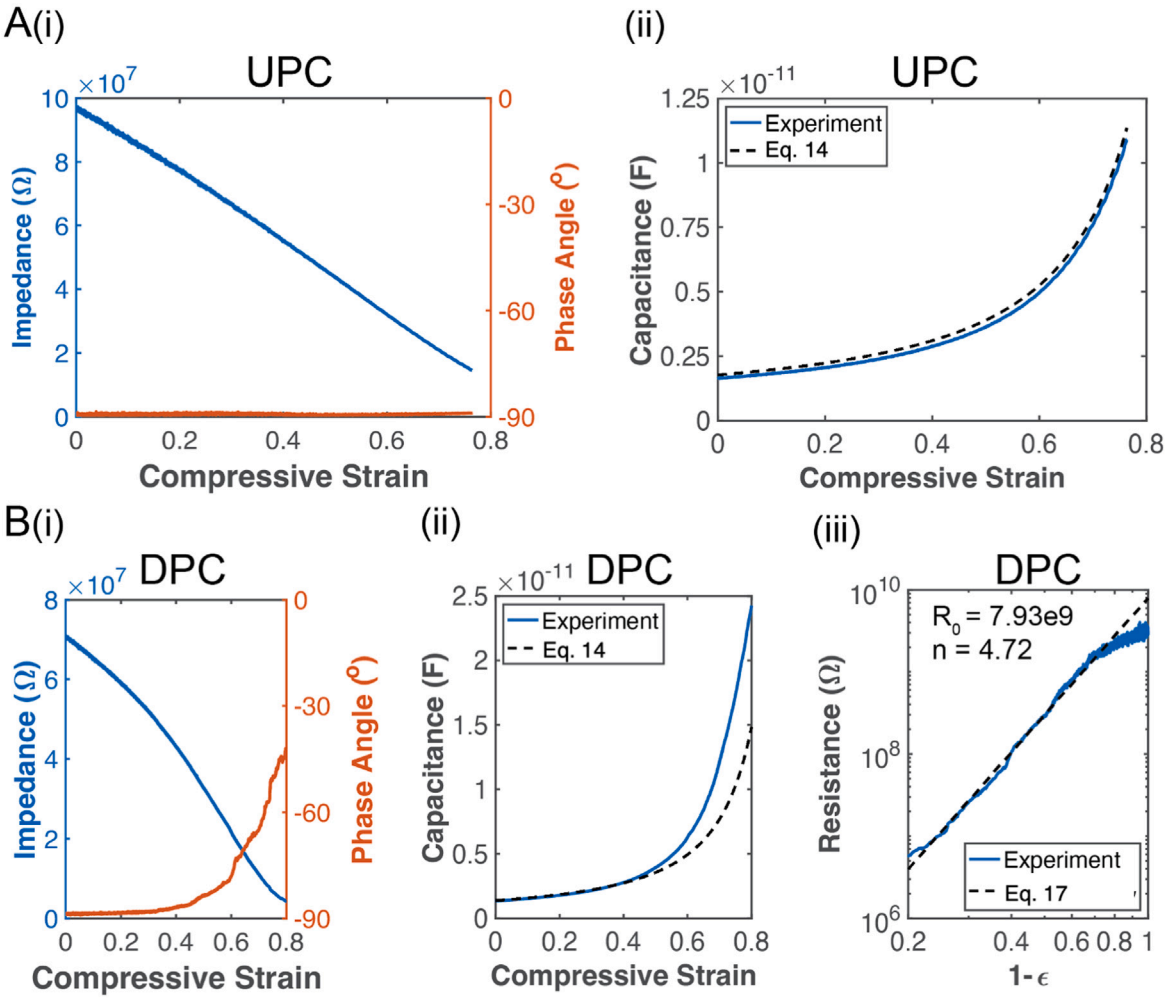

Fig. 6. (A) Results of undoped and uninsulated porous polymer under compression (UPC): (i) Measured impedance magnitude (blue) and phase angle (orange) of UPC; (ii) Measured (blue) and predicted (black dashed) parallel capacitance of UPC. (B) Results of doped and uninsulated PNC under compression (DPC): (i) Measured impedance magnitude (blue) and phase angle (orange) of DPC; (ii) Measured (blue) and predicted (black dashed) parallel capacitance of DPC; (iii) Measured (blue) and Archie's law-fitted (black dashed) parallel resistance of DPC.

3.2. Pressure response

Fig. 6A depicts the electromechanical response of the undoped porous polymer under compression (UPC). The magnitude of the impedance decreases from 96 MΩ to 16 MΩ at an applied engineering strain of 75%. As expected, the phase angle consistently hovers near −90° regardless of the applied strain, indicating the purely capacitive nature of the undoped porous polymer. The measured capacitance of the undoped porous polymer increases from 1.66 pF to 9.95 pF, which is in good agreement with the proposed equivalent circuit model after calibration.

For the doped PNC under compression (DPC), the impedance magnitude has an initial value of around 70 MΩ, which decreases to 4.4 MΩ at an applied compressive strain of 80% (Fig. 6B(i)). In contrast to the undoped porous polymer, the phase angle of the doped PNC increases from −88.7° to −43.2°, indicating a shift from a dielectric to a highly lossy medium under compression. The parallel capacitance of doped PNC agrees well with the proposed mixing law at small to moderate strains (Fig. 6B(ii)). However, the model underestimated the capacitance when the compressive strain is greater than 45%. The discrepancy may be due to the intrinsic dielectrostriction effect of the nanocomposite, that is, k_{NC} changes with compressive stress. Another plausible explanation is the distortion of the electrical field within the PNC due to the increased current flow through the resistive branch as resistance decreases, leading to nonlinear effects. The parallel resistance decreases by more than 500 times from 3 GΩ to 5.7 MΩ. Both the absolute value and the change of magnitude are smaller than our previous work (Ha et al., 2024) because the AC voltage is used to measure the resistance instead of the DC voltage, which eliminates the influence of the contact resistance (Section 4.2). The parallel resistance is almost linear to $1-\epsilon$ on a log–log scale across a broad strain range of 0.2 to 0.8, consistent with Archie's law

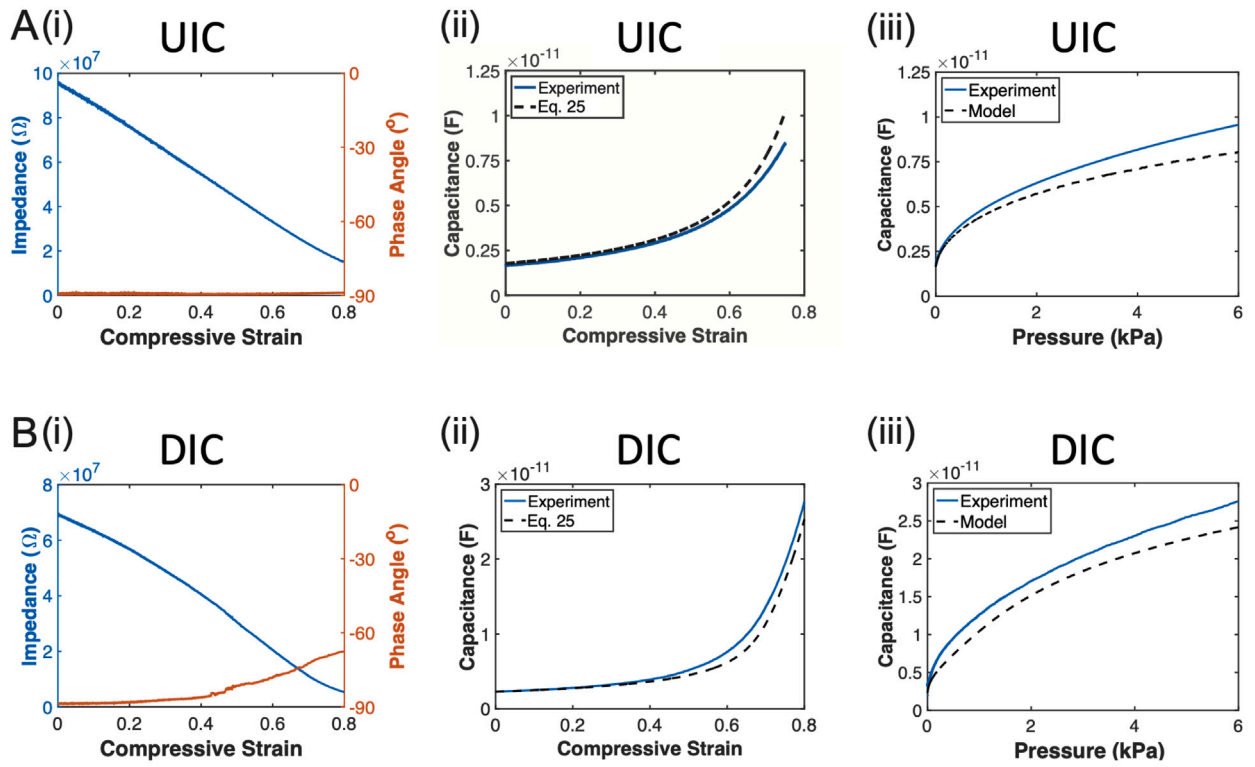

Fig. 7. (A) Results of undoped and insulated porous polymer under compression (UIC): (i) Measured impedance magnitude (blue) and phase angle (orange) of UIC; (ii) Measured (blue) and predicted (black dashed) parallel capacitance of UIC vs. compressive strain; (iii) Measured (blue) and predicted (black dashed) parallel capacitance of UIC vs. applied pressure. (B) Results of doped and insulated PNC under compression (DIC): (i) Measured impedance magnitude (blue) and phase angle (orange) of DIC; (ii) Measured (blue) and predicted (black dashed) parallel capacitance of DIC vs. compressive strain; (iii) Measured (blue) and predicted (black dashed) parallel capacitance of UIC vs. applied pressure.

(Fig. 6B(iii)). However, a different slope was observed at strains below 20%. This discrepancy might be attributed to the inaccurate measurement of resistance when the PNC is almost purely capacitive.

Fig. 7A illustrates the electromechanical response of the undoped and insulated porous polymer under compression (UIC). The behavior of undoped and insulated porous polymer closely resembles that of undoped porous polymer, mainly due to the relatively small thickness of the insulating layer compared to PNC (Fig. 7A). Even under compressive strain of 75%, the thickness of the insulating layer comprises only 0.89% of the specimen, and the impedance of the deformed PNC remains more than 100 times greater than that of the insulating layer. The parallel capacitance is also plotted against compressive stress up to 6 kPa, which roughly corresponds to compressive strain of 80%. In the analytical model, the pressure is obtained by the Ogden–Storakers model in Section 3.1. The results show a satisfactory agreement. The error in the capacitance–pressure relationship is a combination of the errors in the strain–stress and capacitance–strain relationships. In our case, the primary source of error comes from the capacitance–strain relationship.

The impedance magnitude of the doped and insulated PNC under compression (DIC) decreases from 69 MΩ to 5.4 MΩ, a value close to that of the doped PNC alone (Fig. 7B(i)). The phase angle of the insulated doped PNC increases from −88.9° to −67.66°, substantially lower than that of the PNC alone, indicating that the insulating layer keeps the sensor capacitive. Due to the hybrid response, the parallel capacitance of the doped and insulated PNC rises from 2.3 pF to 27 pF, demonstrating a notably higher $\Delta C/C_0$ compared to the undoped counterparts, consistent with our prior research (Ha et al., 2024, 2021). The proposed equivalent circuit model aligns well with the experimental results and exhibits only minor discrepancies at large strains.

3.3. Tension response

The experimental and modeling results of the tensile tests are offered in Fig. 8. The capacitance of undoped porous polymer under tension (UPT) slightly decreases from 3.1 pF to 2.6 pF experimentally under an applied strain of 70%, mainly due to the reduction in effective electrode area and increase in PNC porosity (Fig. 8A(i)). The performance of undoped and insulated porous polymer (UIT) demonstrates a similar trend to UPT (Fig. 8A(ii)). Only capacitance is plotted for undoped specimens because they are purely capacitive. The model agrees reasonably with the experiments..

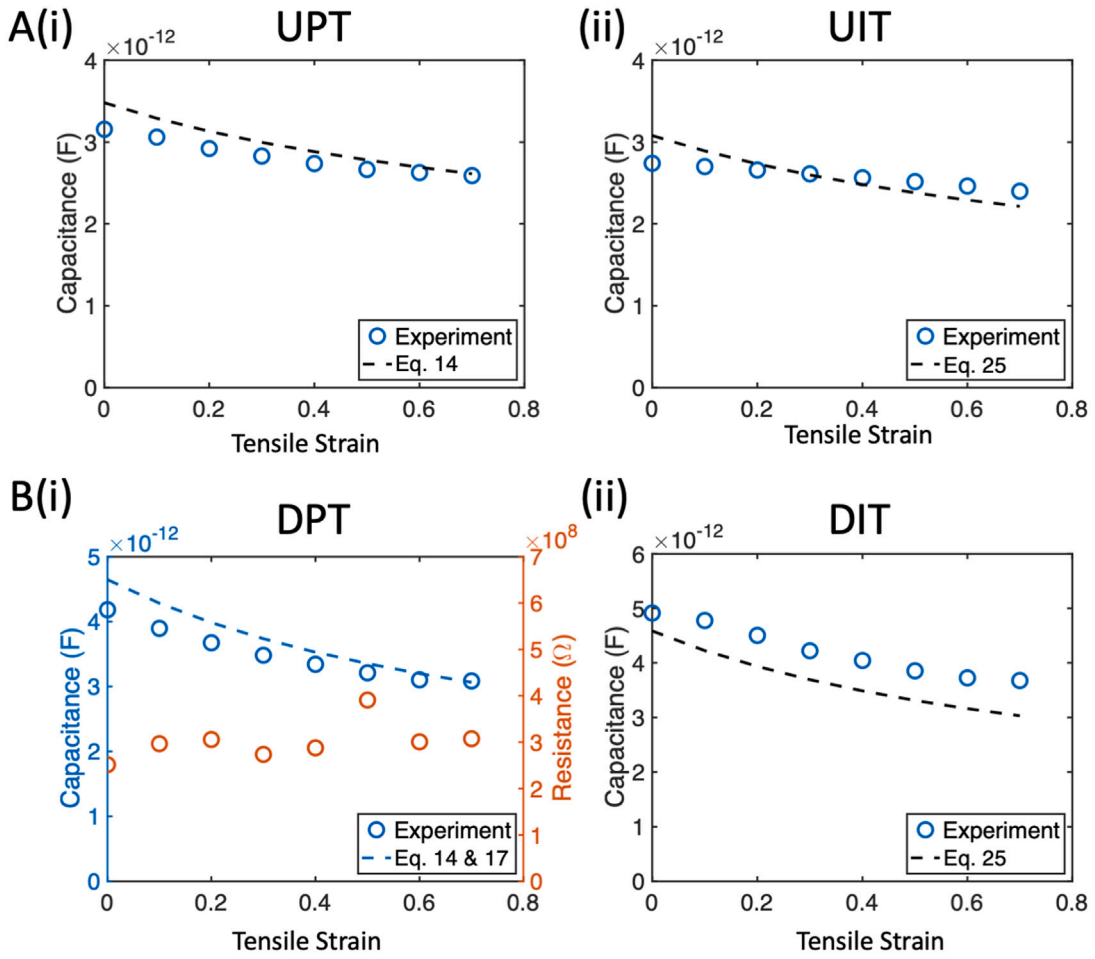

Fig. 8. Experimental and modeling results under in-plane tension for (A) (i) undoped and uninsulated porous polymer (UPT) and (ii) undoped and insulated porous polymer (UIT), (B) (i) doped and uninsulated PNC (DPT) and (ii) doped and insulated PNC (DIT).

For the doped porous nanocomposite (DPT), the capacitance also decreases from 4.2 pF to 3.1 pF (Fig. 8B(i)). The magnitude of the decrease is larger than that of the undoped counterparts because the dielectric constant of the doped nanocomposite is higher than that of the undoped Ecoflex. The parallel resistance remains nearly constant at approximately 300 MΩ under tension, supporting the hypothesis that the resistance is unaffected by the in-plane tensile strain. The hybrid response is not triggered due to the unchanged resistance under tension, causing the doped and insulated PNC (DIT) to behave like a conventional CPS under tension (Fig. 8B(ii)). The capacitance decreases from 5.0 pF to 3.8 pF, which is significantly smaller than the capacitance change under compression (Fig. 7B(ii)).

Results in this work qualitatively align with our previous findings, indicating that the hybrid response is not activated under tension (Ha et al., 2024). However, in this study, the capacitance decreases slightly, whereas it increased in our earlier work. This discrepancy is attributed to the differences in the experimental setup. In the current setup, the effective electrode area decreases because of the fixed top electrode, with the PNC thickness fixed. In contrast, in our previous study, the electrode area increased as the top and bottom electrodes were stretched simultaneously, and the PNC thickness decreased due to the trapped air.

3.4. Shear response

The capacitance of the undoped porous polymer exhibits a small change under an applied shear strain of 100%, indicating intrinsic shear insensitivity in the thin CPS (Fig. 9). This insensitivity is well-captured by our model and is related to the small thickness compared to the electrode width t/a. Note that the electrode distance d, porosity ϕ, and effective dielectric constant k_{eff} remain unchanged during shear according to Eqs. (11), (13), (15), we can express the normalized change of capacitance by rewriting Eq. (15):

$$\frac{\Delta C}{C_0} = \gamma \frac{d_0}{a_0}. \tag{28}$$

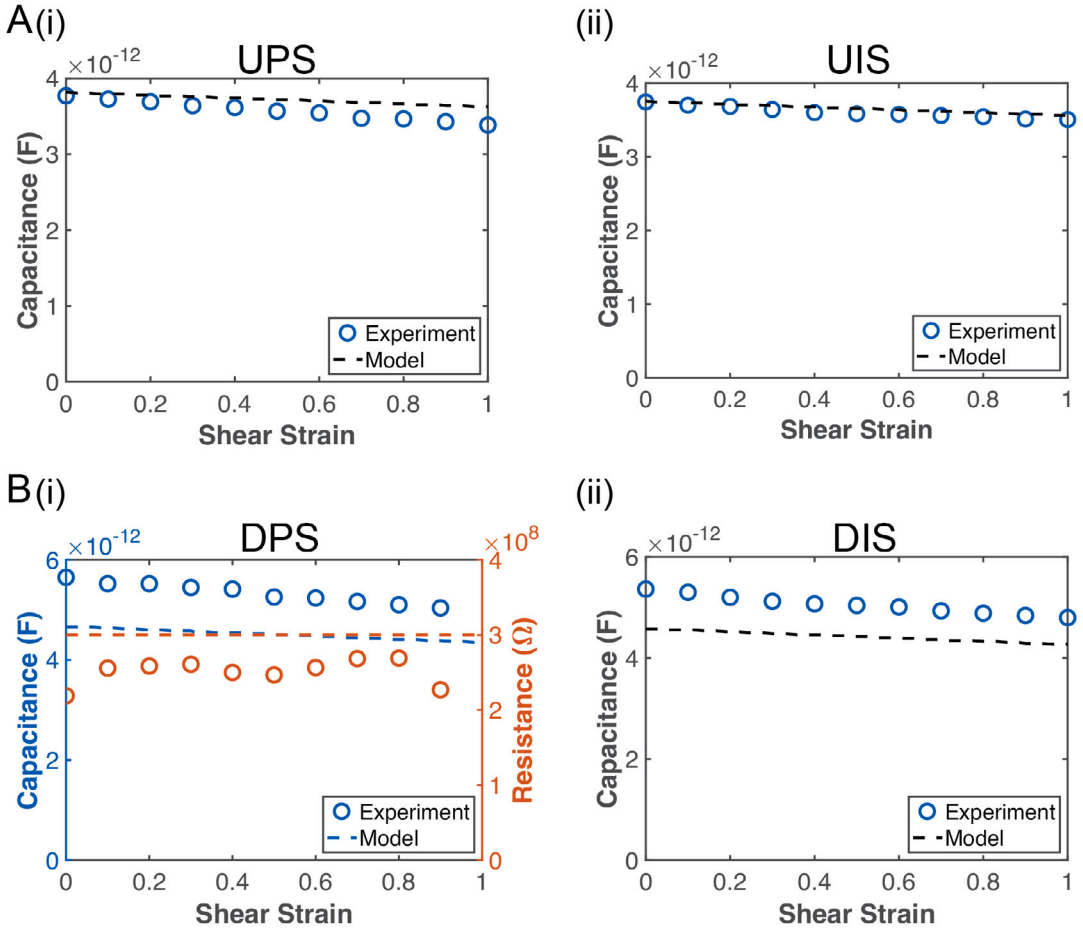

Fig. 9. Experimental and modeling results under shear for (A) undoped and insulated porous polymer (UPS), (B) undoped and insulated porous polymer (UIS), (C) doped and uninsulated PNC (DPS), and (D) doped and insulated PNC (DIS)

In our case, $d_0/a_0 = 0.09$, thus the capacitance changes by only 9% at a shear strain of 100% in our model. Similar to the cases of compression and tension, the electromechanical response of undoped and insulated porous polymer closely mirrors that of undoped porous polymer, primarily because the insulating layer is much thinner than the PNC (Fig. 9A(ii)). The model tends to overestimate the capacitance change, which can be attributed to the fact that the ineffective electrode area–i.e., the electrode area that does not overlap when projected in the normal direction after shear–still contributes to the capacitance through the fringe effect.

Fig. 9B(i) illustrates the parallel capacitance and parallel resistance of the doped PNC under shear. As anticipated by Archie's law, the parallel resistance remains nearly constant because ϕ is preserved. Consequently, the doped PNC does not show a piezoresistive response and behaves similarly to a typical CPS, showing little sensitivity to shear strain. Similarly, the shear response of the doped and insulated PNC is also insensitive to shear strain and exhibits a nearly identical parallel capacitance to that of the PNC only.

4. Discussions

4.1. Choice of equivalent circuit models

This section discusses the selection of models employed for both PNC and insulated PNC. First, we compare six different mixing laws for C_{PNC}, including the parallel model, serial model, Hashin–Shtrikman upper bound (HS+), Hashin–Shtrikman lower bound (HS-), and the Bruggeman model. The parallel model, introduced in Section 2.4.2, represents a microstructure in which the ligaments are prismatic and perpendicular to the electrodes and is similar to the Voigt modulus. The serial model represents an air capacitor connected in series with the NC capacitor, with the parallel capacitance and the effective dielectric constant given by:

$$C^{\mathrm{serial}} = \epsilon_0 k_{\mathrm{eff}}^{\mathrm{serial}} \frac{A}{d}, \quad k_{\mathrm{eff}}^{\mathrm{serial}} = \left(\frac{\phi}{k_{\mathrm{air}}} + \frac{1-\phi}{k_{\mathrm{NC}}} \right)^{-1}. \tag{29}$$

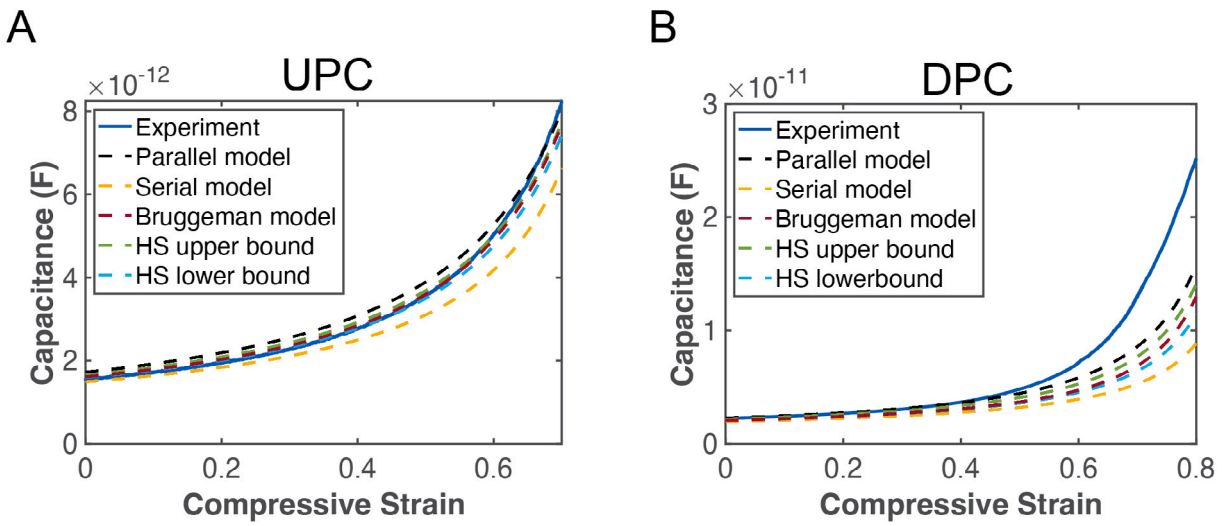

Fig. 10. (A) Different mixing laws for C_{PNC} have small difference and agree relatively well with the experiments for undoped porous polymer. (B) All mixing laws for C_{PNC} underestimate the parallel capacitance of doped PNC at large strain.

The serial model is analogous to the Reuss modulus and represents the effective dielectric constants for a laminar structure. The Hashin–Shtrikman (H-S) upper and lower bounds provide the maximum and minimum values of the effective dielectric constant of a homogeneous mixture. Its value is identical to the well-known Maxwell–Garnett effective medium theory when different components are taken as the filler. The parallel capacitance and the effective dielectric constants of the H-S bounds are expressed as:

$$C^{\mathrm{HS-}} = \epsilon_0 k_{\mathrm{eff}}^{\mathrm{HS-}} \frac{A}{d}, \quad k_{\mathrm{eff}}^{\mathrm{HS-}} = k_{\mathrm{air}} + \frac{k_{\mathrm{air}}(1-\phi)}{\frac{k_{\mathrm{air}}}{k_{\mathrm{NC}}-k_{\mathrm{air}}} + \frac{\phi}{3}}. \tag{30}$$

$$C^{\mathrm{HS+}} = \epsilon_0 k_{\mathrm{eff}}^{\mathrm{HS+}} \frac{A}{d}, \quad k_{\mathrm{eff}}^{\mathrm{HS+}} = k_{\mathrm{NC}} + \frac{k_{\mathrm{NC}}\phi}{\frac{k_{\mathrm{NC}}}{k_{\mathrm{air}}-k_{\mathrm{NC}}} + \frac{1-\phi}{3}}. \tag{31}$$

The Bruggeman model is an effective medium theory widely used in composite materials with parallel capacitance and effective dielectric constant given by:

$$C^{\mathrm{Brug}} = \epsilon_0 k_{\mathrm{eff}}^{\mathrm{Brug}} \frac{A}{d}, \quad k_{\mathrm{eff}}^{Brug} = \frac{1}{4}\left(\beta + \sqrt{\beta^2 + 8k_{\mathrm{air}}k_{\mathrm{NC}}}\right), \quad \beta = (3\phi-1)k_{\mathrm{air}} + (3(1-\phi)-1)k_{\mathrm{NC}}. \tag{32}$$

In all models described above, the porosity ϕ is calculated using Eq. (13). For undoped porous polymer, the differences between the various mixing models are relatively small due to the small difference in k_{air} and k_{NC} (Fig. 10A), and all of them align well with the experimental data. The parallel model yields the largest predicted capacitance, followed by the H-S upper bound, Bruggeman model, H-S lower bound, and serial model in sequence. A greater discrepancy among the models is observed for the doped PNC due to the higher k_{NC} (Fig. 10B). However, all of the models underestimate the capacitance compared to the experiments. The parallel model exhibits the least discrepancy from the experiments as it yields the largest capacitance among all models. Consequently, we chose the parallel model as the mixing law for C_{PNC}.

When constructing the equivalent circuit model for insulated PNC (SHRPS) (Fig. 11A), there are multiple candidates to consider. The simplest model conceptualizes the entire insulating layer as one capacitor connected in series to the PNC (Model 1). The capacitance of the insulating layer C_{IL} is the sum of the three branches of insulating layer introduced in Section 2.4.2, i.e., $C_{\mathrm{IL}} = C_{\mathrm{IL1}} + C_{\mathrm{IL2}} + C_{\mathrm{IL3}}$. The complex impedance and the electrical properties of interest can be written as:

$$Z^{\mathrm{Model1}} = \frac{R_{\mathrm{PNC}}}{1 + i\omega(C_{\mathrm{NC}} + C_{\mathrm{air}})R_{\mathrm{PNC}}} + \frac{1}{i\omega C_{\mathrm{IL}}}. \tag{33}$$

$$Z^{\mathrm{Model1}} = |Z^{\mathrm{Model1}}|, \quad \theta^{\mathrm{Model1}} = \arctan\frac{\mathrm{Im}(Z^{\mathrm{Model1}})}{\mathrm{Re}(Z^{\mathrm{Model1}})}. \tag{34}$$

$$C_{\mathrm{s}}^{\mathrm{Model1}} = \frac{1}{\omega \mathrm{Im}(Z^{\mathrm{Model1}})}, \quad C_{\mathrm{p}}^{\mathrm{Model1}} = \frac{\mathrm{Im}((Z^{\mathrm{Model1}})^{-1})}{\omega}. \tag{35}$$

In a more intricate model (Model 2), we spatially divide the insulating layer into two components: one connecting to the NC (C_{ILA}) and the other connecting to the air (C_{ILB}). This model is motivated by the fact that NC and air possess distinct conductivity and dielectric constants, potentially leading to a nonuniform distribution of electrical potential on the top surface of the insulating

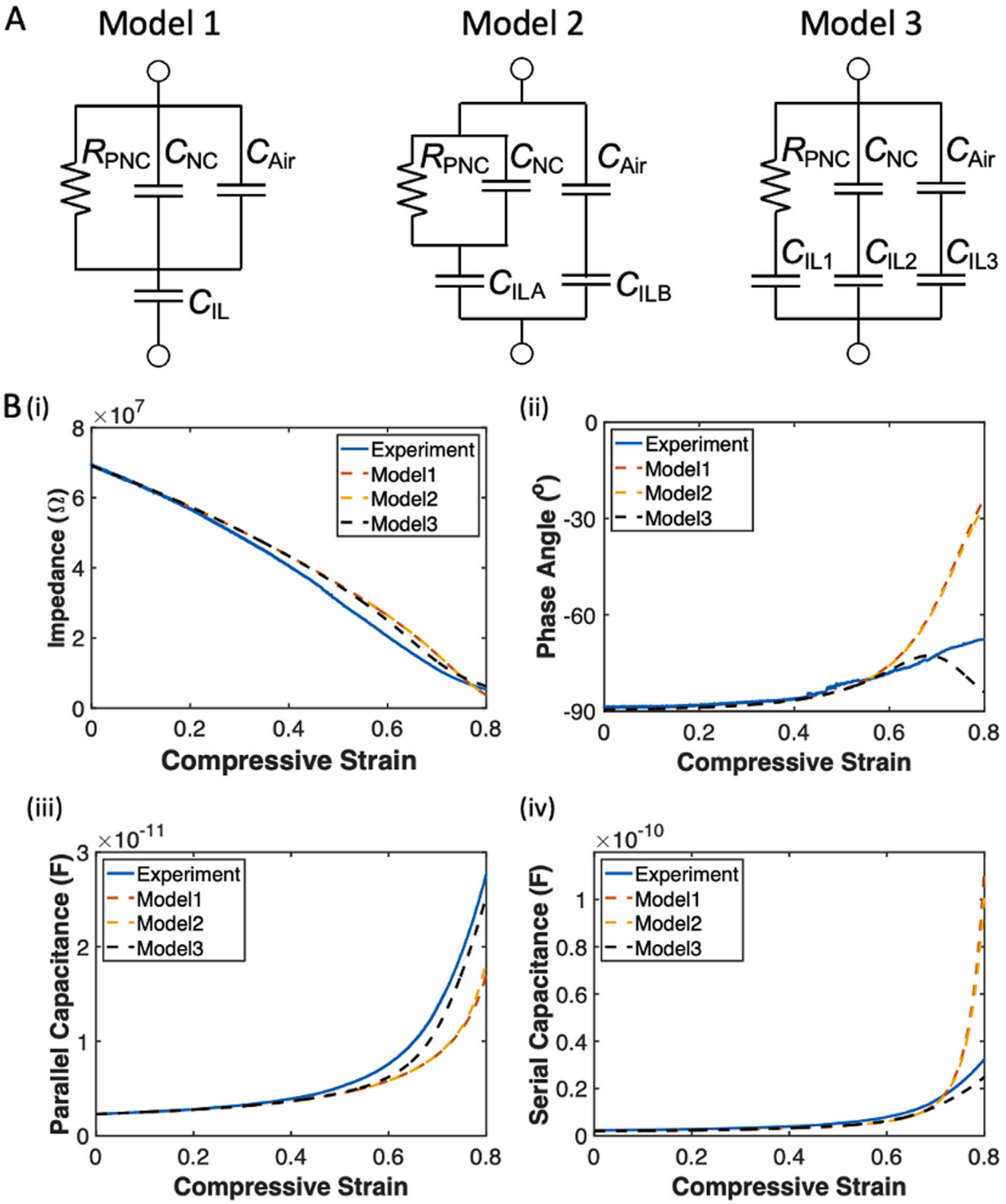

Fig. 11. (A) Three different equivalent circuit models for SHRPS (doped insulated PNC). (B) Comparison between different equivalent circuit models and the experiment for (i) impedance, (ii) phase angle, (iii) parallel capacitance, and (iv) serial capacitance.

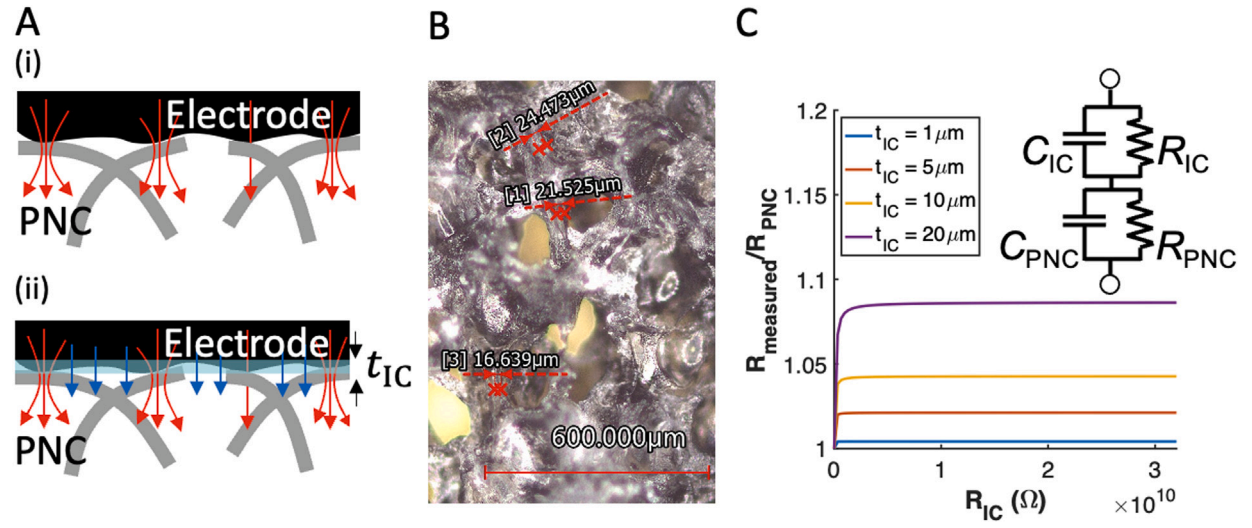

Fig. 12. (A) Schematics showing the effect of incomplete contact on (i) resistance under DC voltage and (ii) impedance under AC voltage. (B) The ligament width of the PNC is measured to be around 20 μm. (C) The contact impedance has little influence on the measured overall impedance of the PNC.

layer. The two components of the insulating layer capacitance are calculated as $C_{\mathrm{ILA}} = C_{\mathrm{IL1}} + C_{\mathrm{IL2}}$, and $C_{\mathrm{ILB}} = C_{\mathrm{IL3}}$. The complex impedance and other electrical properties of model 2 is:

$$Z^{\mathrm{Model2}} = \left[i\omega \frac{C_{\mathrm{air}} C_{\mathrm{IL}}}{C_{\mathrm{air}} + C_{\mathrm{IL}}} + \left(\frac{1}{i\omega C_{\mathrm{IL}}} + \frac{1}{1/R_{\mathrm{PNC}} + i\omega C_{\mathrm{NC}}} \right)^{-1} \right]^{-1}. \tag{36}$$

$$Z^{\mathrm{Model2}} = |Z^{\mathrm{Model2}}|, \quad \theta^{\mathrm{Model2}} = \arctan \frac{\mathrm{Im}(Z^{\mathrm{Model2}})}{\mathrm{Re}(Z^{\mathrm{Model2}})}. \tag{37}$$

$$C_{\mathrm{s}}^{\mathrm{Model2}} = \frac{1}{\omega \mathrm{Im}(Z^{\mathrm{Model2}})}, \quad C_{\mathrm{p}}^{\mathrm{Model2}} = \frac{\mathrm{Im}((Z^{\mathrm{Model2}})^{-1})}{\omega}. \tag{38}$$

We can further split C_{IL1} in Model 2 into two components that connect to C_{NC} and R_{PNC} respectively (Model 3), which is the model presented in the method section. The explicit expressions of electrical properties in model 3 can be found in Section 2.4.3. C_{IL1} and C_{IL2} in Model 3 can be physically interpreted as the insulating layer connecting to the CNTs and the Ecoflex matrix in the NC, respectively.

The impedance predictions provided by these three models agree reasonably well with the experimental measurements (Fig. 11B(i)). However, both Model 1 and Model 2 tend to overestimate the change in phase angle at large strains (Fig. 11B(ii)). Consequently, Model 1 and Model 2 underestimate the parallel capacitance (Fig. 11B(iii)) and overestimate the serial capacitance (Fig. 11B(iv)). Therefore, in this study, we opt for Model 3. These results underscore the importance of carefully examining the nonuniform distribution of electrical potential at the interface between PNC and insulating layers, particularly those caused by the distinct electrical properties of CNT dopants and dielectric matrix.

4.2. Contact impedance

As discussed in the introduction, the interface contact (IC) resistance between the sensing material and the electrode can be the dominant factor in the measured resistance of RPS. However, the influence of contact resistance or contact impedance on the electromechanical properties of SHRPS remains poorly understood. Interfacial contact resistance arises from incomplete contact at the interface, limiting the flow of electrical current through narrow contact points under DC voltage (Fig. 12A(i)). Under AC voltage, alternating current can also traverse through the air, which can be conceptualized as an interfacial capacitance in parallel with the IC resistance (Fig. 12A(ii)). In this study, we estimate the interfacial capacitance as:

$$C_{\mathrm{IC}} = \epsilon_0 k_{\mathrm{PNC}} \frac{A}{t_{\mathrm{IC}}}, \tag{39}$$

where k_{PNC} is estimated using Eq. (15), and t_{IC} is the characteristic length scale of the interfacial contact. In the case of solid materials, t_{IC} is of the same order as the surface roughness. For porous materials, the surface roughness of individual ligaments is challenging to measure, but it should be smaller than the ligament width, which is approximately 20 μm (Fig. 12B). As a rough estimate, we assume that the interfacial impedance is connected in series with the intrinsic PNC impedance.

Fig. 12C depicts the measured parallel resistance versus IC resistance for various values of t_{IC} under the undeformed configuration. For all t_{IC} values investigated, R_{IC} has a negligible effect on the measured parallel resistance of PNC. This small effect of

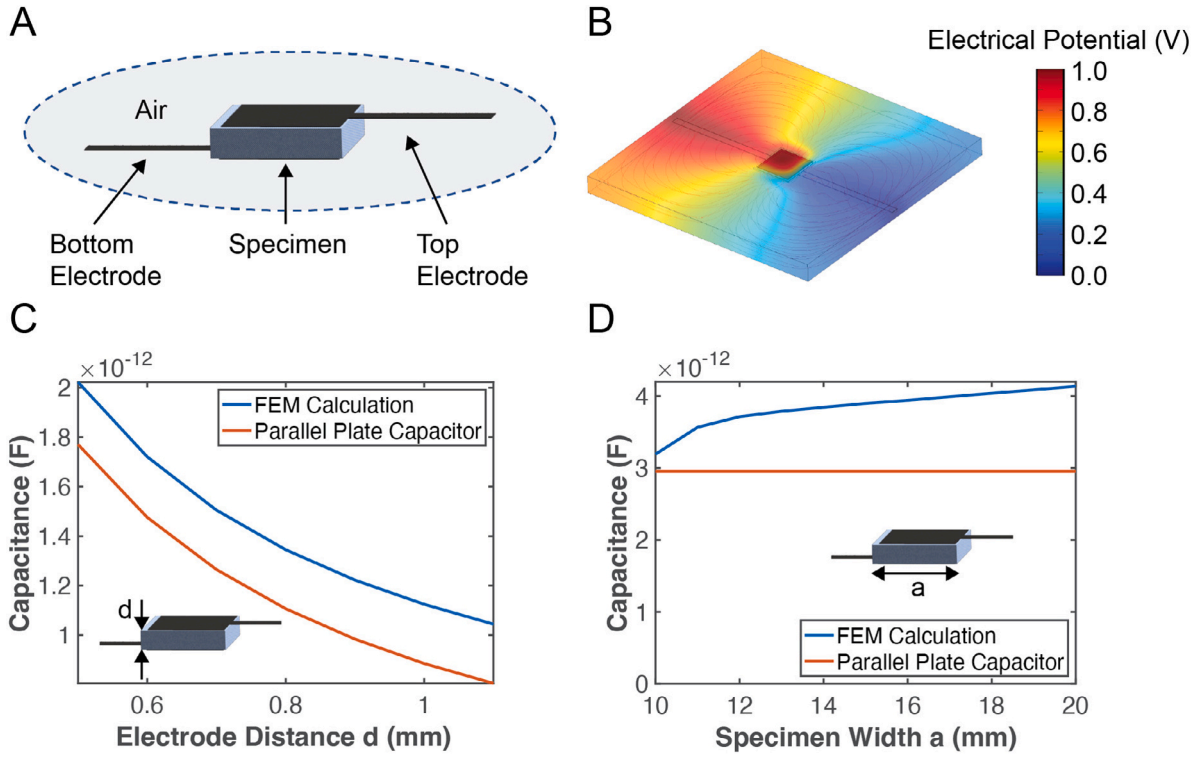

Fig. 13. (A) Geometry of the experimental specimen. (B) The simulated contour of the electrical potential of the specimen and the surrounding air. (C) The fringe effect due to the surrounding air changes little with the change in electrode distance. (D) The fringe effect due to the dimensional mismatch between the electrode and the specimen increases with specimen width.

R_{IC} is due to the fact that $R_{IC} \ll 1/\omega C_{IC}$ in our system and therefore the contact impedance is dominated by the capacitive term. Moreover, $t_{IC} \ll d$, leading to the contact impedance being small compared to the PNC impedance. Consequently, the measured parallel resistance reflects an intrinsic property of the PNC rather than an interfacial property. This finding suggests that the material and structures of the PNC should be optimized rather than focusing on the interface to achieve a hybrid response pressure sensor with improved performance.

4.3. Fringe effect

The fringe effect refers to the influence of the nonuniform electrical field near the edges of the electrodes on the measured capacitance. The fringe effect is inevitable and requires careful calibration for theoretical predictions to align with experimental results. Finite element (FE) simulation was conducted using COMSOL to explore the dependence of the fringe effect on the experimental setup (Fig. 13A). The model comprises a specimen of width a and thickness d. Square electrodes of dimensions 10 mm × 10 mm are attached to the top and bottom surfaces of the specimen, each with a long straight tail of 2 mm width. The bottom electrode is grounded, while the top electrode maintains a constant electrical potential of 1 V. Surrounding air is included in the modeling. As illustrated in the contour of the electrical field (Fig. 13B), the electrical potential experiences a sharp drop along the thickness direction in the specimen but changes slowly in the far fields. The capacitance was extracted from the FE simulation and compared to the equation of parallel plate capacitor $C = \epsilon_0 kA/d$. Fig. 13C illustrates the fringe effect versus the electrode distance d when only air is present. The difference between the FEM calculation and the theory remains almost constant for electrode distances between 0.5 mm and 1 mm, suggesting that a single constant can be used to calibrate the fringe effect during mechanical loading. Fig. 13D displays the fringe effect versus the specimen size a. The fringe effect increases monotonically with specimen width. When $a = 10$ mm, the specimen dimension perfectly matches the electrode, resulting in a minimal fringe effect. However, direct contact between the top and bottom electrodes is likely to occur upon loading and cause a short-circuit for a perfectly matching dimension. In practice, we chose a specimen with $a = 11$ mm for robustness, resulting in an additional fringe effect of approximately 10%.

5. Conclusion

In this study, we systematically characterized the electromechanical behaviors of PNC and insulated PNC under various loading conditions to elucidate the unique behaviors of SHRPS. We propose employing a parallel model to describe the capacitance of the PNC and a directional Archie's law to characterize the parallel resistance of the PNC. In addition, a new equivalent circuit model for insulated PNC (SHRPS) is introduced, which demonstrates good agreement with the experimental findings. We discuss potential sources of errors, including contact impedance and fringe effects. This work provides valuable insights for the future development of SHRPS and can benefit the electromechanical studies of both CPS and RPS based on PNC.

CRediT authorship contribution statement

Zheliang Wang: Writing – original draft, Methodology, Investigation, Formal analysis. **Zhengjie Li:** Writing – original draft, Methodology, Investigation, Formal analysis. **Sungmin Sun:** Investigation, Methodology, Writing – review & editing. **Sangjun Kim:** Writing – review & editing, Methodology, Investigation, Formal analysis. **Xianke Feng:** Investigation. **Hongyang Shi:** Methodology. **Nanshu Lu:** Writing – review & editing, Supervision, Project administration, Funding acquisition, Conceptualization.

Declaration of competing interest

The authors declare the following financial interests/personal relationships which may be considered as potential competing interests: Nanshu Lu reports financial support was provided by National Science Foundation. If there are other authors, they declare that they have no known competing financial interests or personal relationships that could have appeared to influence the work reported in this paper.

Data availability

Data will be made available on request.

Declaration of Generative AI and AI-assisted technologies in the writing process

During the preparation of this manuscript, the authors used ChatGPT to polish the language. After using this tool/service, the authors reviewed and edited the content as needed and assume full responsibility for the content of the publication.

Acknowledgments

We wish to honor and celebrate the 70th birthday of Prof. Wei Yang, whose remarkable insights, mentorship and leadership have had a lasting impact on our research and the broader scientific community.

N.L. acknowledges support from the US NSF ASCENT Grant 2133106 and the US ARO Grant W911NF-24-1-0121.

Appendix A. Supplementary data

Supplementary material related to this article can be found online at https://doi.org/10.1016/j.jmps.2024.105872.

References

Archie, G.E., 1942. The electrical resistivity log as an aid in determining some reservoir characteristics. Trans. AIME 146 (01), 54–62.

Atalay, O., Atalay, A., Gafford, J., Walsh, C., 2018. A highly sensitive capacitive-based soft pressure sensor based on a conductive fabric and a microporous dielectric layer. Adv. Mater. Technol. 3 (1), 1700237.

Casavola, C., Del Core, L., Moramarco, V., Pappalettera, G., Patronelli, M., 2022. Experimental and numerical analysis of the Poisson's ratio on soft polyurethane foams under tensile and cyclic compression load. Mech. Adv. Mater. Struct. 29 (28), 7172–7188.

Chang, Y., Wang, L., Li, R., Zhang, Z., Wang, Q., Yang, J., Guo, C.F., Pan, T., 2021. First decade of interfacial iontronic sensing: from droplet sensors to artificial skins. Adv. Mater. 33 (7), 2003464.

Chen, H., Dejace, L., Lacour, S.P., 2021. Electronic skins for healthcare monitoring and smart prostheses. Annu. Rev. Control Robot. Auton. Syst. 4, 629–650.

Chen, D., Pei, Q., 2017. Electronic muscles and skins: a review of soft sensors and actuators. Chem. Rev. 117 (17), 11239–11268.

Chen, W., Yan, X., 2020. Progress in achieving high-performance piezoresistive and capacitive flexible pressure sensors: A review. J. Mater. Sci. Technol. (ISSN: 1005-0302) 43, 175–188. http://dx.doi.org/10.1016/j.jmst.2019.11.010, URL https://www.sciencedirect.com/science/article/pii/S100503022030044X.

Chortos, A., Liu, J., Bao, Z., 2016. Pursuing prosthetic electronic skin. Nature Mater. (ISSN: 1476-4660) 15 (9), 937–950.

Choy, T.C., 2015. Effective Medium Theory: Principles and Applications, vol. 165, Oxford University Press.

Dascher, D.J., 1996. Measuring parasitic capacitance and inductance using TDR. Hewlett Packard J. 47, 83–96.

Fu, M., Yu, Y., Xie, J., Wang, L., Fan, M., Jiang, S., Zeng, Y., 2009. Significant influence of film thickness on the percolation threshold of multiwall carbon nanotube/low density polyethylene composite films. Appl. Phys. Lett. 94 (1).

Glover, P., 2015. 11.04–Geophysical properties of the near surface earth: Electrical properties. Treatise Geophys. 11, 89–137.

Ha, K.H., Huh, H., Li, Z., Lu, N., 2022. Soft capacitive pressure sensors: trends, challenges, and perspectives. ACS Nano 16 (3), 3442–3448.

Ha, K.H., Li, Z., Kim, S., Huh, H., Wang, Z., Shi, H., Block, C., Bhattacharya, S., Lu, N., 2024. Stretchable hybrid response pressure sensors. Matter 7 (5), 1895–1908.

Ha, K.H., Zhang, W., Jang, H., Kang, S., Wang, L., Tan, P., Hwang, H., Lu, N., 2021. Highly sensitive capacitive pressure sensors over a wide pressure range enabled by the hybrid responses of a highly porous nanocomposite. Adv. Mater. 33 (48), 2103320.

Hammock, M.L., Chortos, A., Tee, B.C.K., Tok, J.B.H., Bao, Z., 2013. 25Th anniversary article: the evolution of electronic skin (e-skin): a brief history, design considerations, and recent progress. Adv. Mater. (ISSN: 0935-9648) 25 (42), 5997–6038.
Khalili, N., Naguib, H., Kwon, R., 2016. A constriction resistance model of conjugated polymer based piezoresistive sensors for electronic skin applications. Soft Matter 12 (18), 4180–4189.
Kim, Y., Chortos, A., Xu, W., Liu, Y., Oh, J.Y., Son, D., Kang, J., Foudeh, A.M., Zhu, C., Lee, Y., Niu, S., Liu, J., Pfattner, R., Bao, Z., Lee, T.W., 2018. A bioinspired flexible organic artificial afferent nerve. Science 360 (6392), 998–1003.
Lee, W.W., Tan, Y.J., Yao, H., Li, S., See, H.H., Hon, M., Ng, K.A., Xiong, B., Ho, J.S., Tee, B.C., 2019. A neuro-inspired artificial peripheral nervous system for scalable electronic skins. Science Robotics 4 (32), eaax2198.
Li, J., Fang, L., Sun, B., Li, X., Kang, S.H., 2020a. Recent progress in flexible and stretchable piezoresistive sensors and their applications. J. Electrochem. Soc. 167 (3), 037561.
Li, Z., Ha, K.H., Wang, Z., Kim, S., Davis, B., Lu, R., Sirohi, J., Lu, N., 2022. Effects of AC frequency on the capacitance measurement of hybrid response pressure sensors. Soft Matter 18 (44), 8476–8485.
Li, Y., Song, A., Qiu, W., Gong, S., Wu, D., Xiao, Z., Jiang, Y., Zhu, Z., 2019. Electrical characterization of flexible CNT/polydimethylsiloxane composite films with finite thickness. Carbon 154, 439–447.
Li, M.Y., Yang, M., Vargas, E., Neff, K., Vanli, A., Liang, R., 2016. Analysis of variance on thickness and electrical conductivity measurements of carbon nanotube thin films. Meas. Sci. Technol. 27 (9), 095004.
Li, S., Zhang, Y., Wang, Y., Xia, K., Yin, Z., Wang, H., Zhang, M., Liang, X., Lu, H., Zhu, M., et al., 2020b. Physical sensors for skin-inspired electronics. InfoMat 2 (1), 184–211.
Lin, C., Wang, H., Yang, W., 2010. Variable percolation threshold of composites with fiber fillers under compression. J. Appl. Phys. 108 (1).
Luo, N., Huang, Y., Liu, J., Chen, S.C., Wong, C.P., Zhao, N., 2017. Hollow-structured graphene–silicone-composite-based piezoresistive sensors: Decoupled property tuning and bending reliability. Adv. Mater. 29 (40), 1702675.
Lv, C., Tian, C., Jiang, J., Dang, Y., Liu, Y., Duan, X., Li, Q., Chen, X., Xie, M., 2023. Ultrasensitive linear capacitive pressure sensor with wrinkled microstructures for tactile perception. Adv. Sci. 10 (14), 2206807.
Mishra, R.B., El-Atab, N., Hussain, A.M., Hussain, M.M., 2021. Recent progress on flexible capacitive pressure sensors: From design and materials to applications. Adv. Mater. Technol. 6 (4), 2001023.
Pierron, F., 2010. Identification of Poisson's ratios of standard and auxetic low-density polymeric foams from full-field measurements. J. Strain Anal. Eng. Des. 45 (4), 233–253.
Pyo, S., Lee, J., Bae, K., Sim, S., Kim, J., 2021. Recent progress in flexible tactile sensors for human-interactive systems: from sensors to advanced applications. Adv. Mater. 33 (47), 2005902.
Qin, J., Yin, L.J., Hao, Y.N., Zhong, S.L., Zhang, D.L., Bi, K., Zhang, Y.X., Zhao, Y., Dang, Z.M., 2021. Flexible and stretchable capacitive sensors with different microstructures. Adv. Mater. 33 (34), 2008267.
Ruth, S.R.A., Beker, L., Tran, H., Feig, V.R., Matsuhisa, N., Bao, Z., 2020. Rational design of capacitive pressure sensors based on pyramidal microstructures for specialized monitoring of biosignals. Adv. Funct. Mater. 30 (29), 1903100.
Storåkers, B., 1986. On material representation and constitutive branching in finite compressible elasticity. J. Mech. Phys. Solids 34 (2), 125–145.
Tang, Z., Jia, S., Zhou, C., Li, B., 2020. 3D printing of highly sensitive and large-measurement-range flexible pressure sensors with a positive piezoresistive effect. ACS Appl. Mater. Interfaces 12 (25), 28669–28680.
Wang, X., Dong, L., Zhang, H., Yu, R., Pan, C., Wang, Z.L., 2015. Recent progress in electronic skin. Adv. Sci. 2 (10), 1500169.
Wang, M., Luo, Y., Wang, T., Wan, C., Pan, L., Pan, S., He, K., Neo, A., Chen, X., 2021. Artificial skin perception. Adv. Mater. 33 (19), 2003014.
Wang, S., Oh, J.Y., Xu, J., Tran, H., Bao, Z., 2018. Skin-inspired electronics: an emerging paradigm. Acc. Chem. Res. 51 (5), 1033–1045.
Yang, J.C., Mun, J., Kwon, S.Y., Park, S., Bao, Z., Park, S., 2019. Electronic skin: recent progress and future prospects for skin-attachable devices for health monitoring, robotics, and prosthetics. Adv. Mater. 31 (48), 1904765.
Yang, J., Tang, D., Ao, J., Ghosh, T., Neumann, T.V., Zhang, D., Piskarev, Y., Yu, T., Truong, V.K., Xie, K., Lai, Y.C., Li, Y., Dickey, M.D., 2020a. Ultrasoft liquid metal elastomer foams with positive and negative piezopermittivity for tactile sensing. Adv. Funct. Mater. 30 (36), 2002611.
Yang, H., Yuan, L., Yao, X., Fang, D., 2020b. Piezoresistive response of graphene rubber composites considering the tunneling effect. J. Mech. Phys. Solids 139, 103943.
Yao, S., Zhu, Y., 2014. Wearable multifunctional sensors using printed stretchable conductors made of silver nanowires. Nanoscale 6 (4), 2345–2352.
Yuan, X., Won, S.M., Han, M., Wang, Y., Rogers, J.A., Huang, Y., Wang, H., 2021. Mechanics of encapsulated three-dimensional structures for simultaneous sensing of pressure and shear stress. J. Mech. Phys. Solids 151, 104400.
Zhang, J., Wang, Z., Peng, Z., 2021. Analytical model of the piezoresistive behavior of highly compressible sensors made of microporous nanocomposites. Adv. Theory Simul. 4 (12), 2100247.
Zhang, Y., Yang, J., Hou, X., Li, G., Wang, L., Bai, N., Cai, M., Zhao, L., Wang, Y., Zhang, J., et al., 2022. Highly stable flexible pressure sensors with a quasi-homogeneous composition and interlinked interfaces. Nature Commun. 13 (1), 1317.